CHAPTER

8

EXPERIMENTAL NMR RELAXATION METHODS

The basics of the theory of spin relaxation in NMR spectroscopy are presented in Chapter 5 and aspects of relaxation important for the design of particular NMR experiments are discussed in Chapters 6 and 7. This chapter describes spin relaxation experiments for characterizing dynamic properties of molecules over a range of different time scales with atomic resolution (*1*). Applications of these methods include investigations of backbone and side chain conformational dynamics of multiple functional states of proteins in order to characterize folding, stability, binding, and catalysis (*2*). The development of new experiments for probing molecular dynamic properties is an active area of investigation, and novel methods continue to be described in the literature on a regular basis. The experiments described in this chapter largely report on the local dynamics of a single spin or a pair of directly bonded spins. Relaxation interference between different stochastic Hamiltonians results from correlated dynamic processes (Sections 5.2.1 and 5.45). Development of comprehensive and sensitive methods for investigating correlated motions in proteins represents a particularly important area of current research (*3*).

The time scale of a dynamic process that can be characterized by spin relaxation methods depends directly on the magnitude of the variation in the spin Hamiltonian modulated by the dynamic process.

Thus, motions on picosecond–nanosecond time scales are accessible to spin relaxation resulting from modulation of dipole–dipole (DD), chemical shift anistropy (CSA), and quadrupolar Hamiltonians, as discussed in Section 5.4. Motions on microsecond–millisecond time scales are accessible to spin relaxation resulting from modulation of isotropic chemical shifts, that is, from chemical exchange phenomena, as discussed in Section 5.6. The magnitude of the variation in isotropic scalar coupling constants in proteins, on the order of 10 Hz, is too small to have proved useful as a direct relaxation probe of molecular dynamics in macromolecules; however, observation of averaged values of scalar coupling constants provides evidence of dynamic processes that are too fast to serve as efficient relaxation mechanisms, as discussed in Section 5.6.2. A number of comprehensive reviews of these methods and applications are available (*4–9*).

8.1 Pulse Sequences and Experimental Methods

Pulse sequences for measuring spin relaxation usually consist of five building blocks: preparation, relaxation, frequency labeling, mixing, and acquisition. In some cases, frequency labeling may occur before the relaxation period or pairs of building blocks may be combined. Insertion of the relaxation period is the only difference from other types of two-dimensional NMR spectroscopy, discussed in Section 4.1. Thus, preparation, frequency labeling, and mixing steps can be performed using the range of approaches described in other chapters. For homonuclear ^{1}H experiments, the preparation period normally consists of a 90° pulse and the mixing period consists of a 90° pulse or a TOCSY sequence (Section 6.5). For heteronuclear experiments, the preparation period consists of an INEPT (Sections 2.7.7.2 and 2.7.7.3) or NOE (Section 5.5) transfer step from ^{1}H spins to the nucleus of interest and the mixing period consists of INEPT, PEP (Section 7.1.3.2), or TROSY (Chapter 7) sequences. The density operator present after the preparation period provides the initial condition for the relaxation period, T. Two-dimensional Fourier transformation yields a frequency-domain spectrum in which the relaxation information is encoded in the intensities or lineshapes of the resonance signals.

The prototypical situation that arises in the design of experimental methods for measuring relaxation rate constants consists of two eigenoperators, **A** and **B**, with eigenfrequencies Ω_A and Ω_B that are subject to autorelaxation, with rate constants ρ_A and ρ_B, respectively,

and cross-relaxation, with rate constant η:

$$\frac{d}{dt}\begin{bmatrix}\langle A\rangle(t)\\ \langle B\rangle(t)\end{bmatrix}=\begin{bmatrix}i\Omega_A-\rho_A & -\eta\\ -\eta & i\Omega_B-\rho_B\end{bmatrix}\begin{bmatrix}\langle A\rangle(t)-\langle A\rangle^0\\ \langle B\rangle(t)-\langle B\rangle^0\end{bmatrix}, \qquad [8.1]$$

in which $\langle A\rangle(t)=\mathrm{Tr}\{\mathbf{A}\sigma(t)\}$, and $\langle A\rangle^0$ is the equilibrium expectation value; similar expressions hold for **B**. The formal solution to this equation is, for a relaxation period T,

$$\begin{bmatrix}\langle A\rangle(T)\\ \langle B\rangle(T)\end{bmatrix}=\begin{bmatrix}\langle A\rangle^0\\ \langle B\rangle^0\end{bmatrix}+\exp\left\{T\begin{bmatrix}i\Omega_A-\rho_A & -\eta\\ -\eta & i\Omega_B-\rho_B\end{bmatrix}\right\}\begin{bmatrix}\langle A\rangle(0)-\langle A\rangle^0\\ \langle B\rangle(0)-\langle B\rangle^0\end{bmatrix}. \qquad [8.2]$$

Aspects of these equations have been discussed at length in Chapter 5 (in particular, Sections 5.1.2, 5.5.2, and 5.6) and are recapitulated here. If **A** and **B** are not secular, typically due to resolved scalar coupling and chemical shift interactions, so that $|\Omega_A-\Omega_B|\gg\rho_A$, ρ_B, and η, then the effects of η vanish and each basis operator relaxes independently with rate constants ρ_A and ρ_B. If **A** and **B** are secular, then relaxation is biexponential with rate constants that depend on the eigenvalues of the relaxation rate matrix. Multiexponential intensity decay curves are difficult to resolve experimentally and accurate measurements of ρ_A, ρ_B, and η based on [8.2] are not easily achieved. In the initial rate regime,

$$\begin{bmatrix}\langle A\rangle(T)\\ \langle B\rangle(T)\end{bmatrix}\approx\begin{bmatrix}\langle A\rangle(0)\\ \langle B\rangle(0)\end{bmatrix}+T\begin{bmatrix}i\Omega_A-\rho_A & -\eta\\ -\eta & i\Omega_B-\rho_B\end{bmatrix}\begin{bmatrix}\langle A\rangle(0)-\langle A\rangle^0\\ \langle B\rangle(0)-\langle B\rangle^0\end{bmatrix}. \qquad [8.3]$$

If selective excitation or inversion of the operator **A** is possible, so that $\langle B\rangle(0)=\langle B\rangle^0$, then ρ_A is obtained from the initial decay of $\langle A\rangle(T)$ and η is obtained from the initial buildup of $\langle B\rangle(T)$. Analogous results are obtained if selective perturbation of **B** is possible.

Experimental manipulations during T commonly are utilized to affect the relaxation behavior predicted by [8.1] and [8.2]. Such manipulations fall into two categories: (*i*) application of rf fields that introduce a new time dependence to spin evolution and alter whether operators are secular and (*ii*) pulse sequence elements that provide a desired average relaxation behavior. Examples of these approaches are given in the following discussion, assuming that **A** and **B** are secular with $\Omega_A=\Omega_B=0$ in the rotating frame.

As an example of the first category, if the operator **B** is saturated (Section 5.1.2), then **A** relaxes independently according to

$$\frac{d\langle A\rangle(t)}{dt} = -\rho_A\left[\langle A\rangle(t) - \langle A\rangle^{SS}\right], \qquad [8.4]$$

in which the steady-state expectation value of **A** is given by

$$\langle A\rangle^{SS} = \langle A\rangle^0\left(1 + \frac{\eta\langle B\rangle^0}{\rho_A\langle A\rangle^0}\right). \qquad [8.5]$$

As a second example, if the operators **A** and **B** are spin-locked, either by application of a continuous-wave rf field or by a train of pulses, then the operators can become secular in the rotating frame of reference and ROESY-like cross-relaxation pathways become active (Section 5.4.3).

As an example of the second category, if two experiments are recorded in which $\langle A\rangle_1(0) = -\langle A\rangle_2(0) = \langle A\rangle(0)$, and with similar expressions for **B**, then the average relaxation decay obtained by subtracting the two data sets is described by

$$\begin{bmatrix}\langle A\rangle(T)\\ \langle B\rangle(T)\end{bmatrix} = \frac{1}{2}\left\{\begin{bmatrix}\langle A\rangle_1(T)\\ \langle B\rangle_1(T)\end{bmatrix} - \begin{bmatrix}\langle A\rangle_2(T)\\ \langle B\rangle_2(T)\end{bmatrix}\right\} = \exp\left\{-T\begin{bmatrix}\rho_A & \eta\\ \eta & \rho_B\end{bmatrix}\right\}\begin{bmatrix}\langle A\rangle(0)\\ \langle B\rangle(0)\end{bmatrix}, \qquad [8.6]$$

and the contribution of the equilibrium values of the basis operators has been eliminated. As a second example, consider the sequence $T/2$–**U**–$T/2$, in which

$$\mathbf{U} = \begin{bmatrix}1 & 0\\ 0 & -1\end{bmatrix} \qquad [8.7]$$

represents an inversion operation for **B** and an identity operation for **A**. If $\eta T \ll 1$, then, ignoring the equilibrium expectation values, the average evolution during time T is given by

$$\begin{aligned}\mathbf{U}^{-1}\mathbf{M}(T) &= \mathbf{U}^{-1}\exp\left\{-\frac{T}{2}\begin{bmatrix}\rho_A & \eta\\ \eta & \rho_B\end{bmatrix}\right\}\mathbf{U}\exp\left\{-\frac{T}{2}\begin{bmatrix}\rho_A & \eta\\ \eta & \rho_B\end{bmatrix}\right\}\mathbf{M}(0)\\ &= \exp\left\{-\frac{T}{2}\mathbf{U}^{-1}\begin{bmatrix}\rho_A & \eta\\ \eta & \rho_B\end{bmatrix}\mathbf{U}\right\}\exp\left\{-\frac{T}{2}\begin{bmatrix}\rho_A & \eta\\ \eta & \rho_B\end{bmatrix}\right\}\mathbf{M}(0)\\ &\approx \exp\left\{-\frac{T}{2}\left(\mathbf{U}^{-1}\begin{bmatrix}\rho_A & \eta\\ \eta & \rho_B\end{bmatrix}\mathbf{U} + \begin{bmatrix}\rho_A & \eta\\ \eta & \rho_B\end{bmatrix}\right)\right\}\mathbf{M}(0)\\ &\approx \exp\left\{-T\begin{bmatrix}\rho_A & 0\\ 0 & \rho_B\end{bmatrix}\right\}\mathbf{M}(0), \qquad [8.8]\end{aligned}$$

in which $\mathbf{U}^{-1}\mathbf{M}(T) = [\langle A\rangle(T), -\langle B\rangle(T)]^T$. In this case, the effect of cross-relaxation is suppressed to first order in time and the resulting equations then yield independent, monoexponential relaxation decays for both operators **A** and **B**. More complex pulsing schemes can provide a higher degree of suppression if necessary (*10*).

In the preceding examples, relaxation of the desired operator is monoexponential, either by nature of the secular approximation or by pulse sequence manipulations. Consequently, the intensity of the resonance signal is described by

$$\langle A\rangle(T) = \langle A\rangle(0)\,\exp(-\rho_A T). \qquad [8.9]$$

Most commonly, the rate constant is determined by curve fitting this equation to a time series $\langle A\rangle(T)$ recorded for a range of values of T. A minimum of two time points is required, in which case,

$$\rho_A = (1/T)\,\ln[\langle A\rangle(0)/\langle A\rangle(T)]. \qquad [8.10]$$

Strategies for optimal sampling have been investigated thoroughly (*11, 12*). In accordion spectroscopy (*13–16*), the relaxation delay is varied in concert with the frequency-labeling period according to $T = \kappa t_1$, in which κ is a constant. The relaxation rate constant is encoded into the time decay of the t_1 interferogram, or the F_1 linewidth.

A powerful approach for measuring cross-relaxation rate constants utilizes the sequence $T/2$–**U**–$T/2$, in which the propagator **U** interchanges A and B (*17*):

$$\mathbf{U} = \begin{bmatrix} 0 & 1 \\ 1 & 0 \end{bmatrix}. \qquad [8.11]$$

The average evolution over the sequence is

$$\begin{aligned}
\mathbf{U}^{-1}\mathbf{M}(T) &= \mathbf{U}^{-1}\exp\left\{-\frac{T}{2}\begin{bmatrix}\rho_A & \eta\\ \eta & \rho_B\end{bmatrix}\right\}\mathbf{U}\exp\left\{-\frac{T}{2}\begin{bmatrix}\rho_A & \eta\\ \eta & \rho_B\end{bmatrix}\right\}\mathbf{M}(0)\\
&= \exp\left\{-\frac{T}{2}\mathbf{U}^{-1}\begin{bmatrix}\rho_A & \eta\\ \eta & \rho_B\end{bmatrix}\mathbf{U}\right\}\exp\left\{-\frac{T}{2}\begin{bmatrix}\rho_A & \eta\\ \eta & \rho_B\end{bmatrix}\right\}\mathbf{M}(0)\\
&\approx \exp\left\{-\frac{T}{2}\left(\mathbf{U}^{-1}\begin{bmatrix}\rho_A & \eta\\ \eta & \rho_B\end{bmatrix}\mathbf{U} + \begin{bmatrix}\rho_A & \eta\\ \eta & \rho_B\end{bmatrix}\right)\right\}\mathbf{M}(0)\\
&\approx \exp\left\{-T\begin{bmatrix}\overline{\rho} & \eta\\ \eta & \overline{\rho}\end{bmatrix}\right\}\mathbf{M}(0), \qquad [8.12]
\end{aligned}$$

in which $\overline{\rho} = [\rho_A + \rho_B]/2$. In this equation, $\mathbf{U}^{-1}\mathbf{M}(T) = [\langle B\rangle(T), \langle A\rangle(T)]^T$; therefore, the amplitude $\langle A\rangle(T)$ is encoded into the intensity of the operator **B** in the final spectrum, and *vice versa*. If the initial state of the density operator is proportional to **A** and the magnitude of $\langle A\rangle(T)$ and $\langle B\rangle(T)$ are recorded in separate experiments after the relaxation period, then

$$\langle B\rangle(T)/\langle A\rangle(T) = \tanh(\eta T). \qquad [8.13]$$

The propagator **U** may reflect evolution under the scalar coupling Hamiltonian or a designed pulse sequence element. Equation [8.12] is symmetrical, so identical results are obtained if the initial state of the density operator is proportional to **B**, except that **A** and **B** are swapped in [8.13]. Performing the experiment twice with the different initial conditions can be useful in compensating for imperfections in the experimental methods, a technique that has been called "symmetrical reconversion" (*18*).

The hallmark of relaxation interference is that different components of scalar-coupled multiplets relax at different rates. Accordingly, interference relaxation rate constants can be obtained from analysis of the linewidths or intensities of multiplets in frequency-domain NMR spectra, as an alternative to the time-domain analysis of [8.13] (*19–21*). If the scalar couplings are resolved, then the multiplet components are nonsecular with respect to each other and relax independently (Sections 5.4.2 and 5.4.5). For simplicity, a scalar-coupled doublet is considered. Evolution is described by [5.146]:

$$\frac{d}{dt}\begin{bmatrix}\langle I^+S^\alpha\rangle(t)\\ \langle I^+S^\beta\rangle(t)\end{bmatrix} = -\begin{bmatrix} i\pi J_{IS} + \overline{R}_2 + \eta_{xy} & 0\\ 0 & -i\pi J_{IS} + \overline{R}_2 - \eta_{xy}\end{bmatrix}\begin{bmatrix}\langle I^+S^\alpha\rangle(t)\\ \langle I^+S^\beta\rangle(t)\end{bmatrix}. \qquad [8.14]$$

At the end of a constant-time evolution period of length T, the intensities of the two doublet components are given by

$$\begin{aligned}\langle I^+S^\alpha\rangle(T) &= \tfrac{1}{2}\langle I^+\rangle(0)\,\exp\left[-\left(\overline{R}_2 + \eta_{xy}\right)T\right],\\ \langle I^+S^\beta\rangle(T) &= \tfrac{1}{2}\langle I^+\rangle(0)\,\exp\left[-\left(\overline{R}_2 - \eta_{xy}\right)T\right],\end{aligned} \qquad [8.15]$$

in which $\langle I^+\rangle(0) = \langle I^+S^\alpha\rangle(0) + \langle I^+S^\beta\rangle(0)$ is the total initial intensity of the doublet — that is, the in-phase magnetization. Accordingly, the relaxation interference rate constant is obtained from the measured

doublet intensities as

$$\eta_{xy} = \frac{1}{2T} \ln\left[\frac{\langle I^+ S^\beta\rangle(T)}{\langle I^+ S^\alpha\rangle(T)}\right]. \qquad [8.16]$$

This approach is particularly powerful for more complex spin systems, such as $^{13}CH_2$ moieties (*20*), or multiple-quantum coherences (*19, 21*).

The preceding manipulations will be utilized in various combinations in the pulse sequences described next. In many of these methods, the number of pulses applied during T will increase as T increases. Consequently, systematic errors result if the pulses have unintended effects on the density operator. For example, application of increasing numbers of ^1H pulses can lead to progressive saturation of the water resonance. Saturation transfer from water to amide $^1H^N$ spins by amide proton solvent exchange will occur during the recycle delay for fast-exchanging amide sites. As a result, the initial value of the $^1H^N$ magnetization will depend on T, and relaxation rate constants will be overestimated. These errors can be avoided by using gradients to completely dephase the water resonance at the start of the recycle delay, at a cost of reduced sensitivity for fast-exchanging spins (Section 3.5), by using recycle delays $> 3/R_{1w}$, in which R_{1w} is the longitudinal relaxation rate constant for the water resonance, or by using carefully optimized water flip-back methods (Section 3.5). Most of the pulse sequences illustrated in the following discussions will use the first approach; consequently, the experiments shown for ^{15}N backbone amide nuclear spins also are applicable to other X nuclei in isolated *IS* spin systems. Water flip-back approaches for spin relaxation methods are discussed elsewhere (*22*). As another example, heating of the sample may occur as T increases because the amount of rf power deposited into the sample increases with the number of applied pulses or with the length of spin-locking and decoupling sequences. Because relaxation rate constants are highly temperature sensitive, severe systematic errors can result. To avoid such errors, the field strength of applied rf fields may need to be reduced and compensatory pulses should be applied during the recycle delay to ensure that the rf power deposited into the sample is independent of T (*23*).

8.2 Picosecond–Nanosecond Dynamics

Techniques for probing picosecond–nanosecond time scale motions rely upon the DD and CSA relaxation mechanisms for ^1H, ^{13}C, and ^{15}N

spins and the quadrupolar relaxation mechanisms for ^{2}H (= D) spins. The following sections describe experiments for measuring relaxation rate constants for backbone amide ^{15}N spins, ^{2}H spins in side chain CH_2D groups, and backbone carbonyl ^{13}C spins.

8.2.1 EXPERIMENTAL METHODS FOR ^{15}N LABORATORY-FRAME RELAXATION

Experimental methods have been developed extensively for R_1, R_2, and NOE measurements of backbone and side chain ^{15}N nuclear spins in proteins (*22, 24–26*). Illustrative pulse sequences for measuring backbone amide ^{15}N spin relaxation in proteins are shown in Fig. 8.1. These experiments are based on the HSQC pulse sequence (Section 7.1.1) and are easily modified for larger proteins using the TROSY technique (*27*). These sequences can be adapted to measurements of side chain amide ^{15}N spin relaxation (*24*), and for ^{1}H–^{13}C *IS* spin systems in which ^{13}C–^{13}C scalar coupling and dipolar interactions are negligible, such as in naturally abundant (*28*), fractionally enriched (*29*), or alternately labeled (*30*) samples.

The inversion-recovery technique (*31*) is used to measure the spin–lattice relaxation rate constant for longitudinal magnetization, R_1. This experiment uses a refocused INEPT sequence for the preparation period. Thus, the density operator at the beginning of the relaxation period, T, is proportional to S_z. Phase alternation of ϕ_1 in Fig. 8.1a alternates the sign of the S_z magnetization and consequently suppresses the contribution to relaxation from the equilibrium or steady-state magnetization. Decoupling of the ^{1}H spins during the relaxation period T is used to suppress ^{1}H–^{15}N dipolar cross-relaxation and ^{1}H–^{15}N DD/^{15}N CSA relaxation interference (*32*). Decoupling is accomplished by applying a train of 180° pulses spaced at short, typically 5-ms intervals. The intensity decay is described by

$$\langle S_z\rangle(T) = \langle S_z\rangle(0)\,\exp(-R_1 T). \qquad [8.17]$$

Either the Carr–Purcell–Meiboom–Gill (CPMG) (*33, 34*) or the $R_{1\rho}$ (*35*) technique is used to measure the spin–spin relaxation rate constant for transverse magnetization, R_2. Even though rf fields are applied to the S spins during T in these pulse sequences, the average amplitudes of the fields are sufficiently weak that $J(\omega \pm \omega_e) = J(\omega)$ for the dipole–dipole and CSA relaxation mechanisms, and the relaxation rate constants are not affected by the rf fields. This situation is different for slower chemical exchange processes discussed in Section 8.3. The CPMG

R_2 experiment shown in Fig. 8.1b uses a refocused INEPT sequence for the preparation period. Thus, the density operator at the beginning of the relaxation period, T, is proportional to S_x. Cross-relaxation due to ^1H–^{15}N DD/^{15}N CSA relaxation interference is suppressed by applying 180° ^1H pulses. These pulses are applied after an even-numbered spin echo so as not to interfere with the compensating effects of the CPMG pulse train (*36, 37*). The intensity decay is described by

$$\langle S_x \rangle(T) = \langle S_x \rangle(0) \exp(-R_2 T), \qquad [8.18]$$

in which $T = 2n\tau_{cp}$, $2n$ is the number of spin echo periods, and τ_{cp} is the length of a single spin echo period. An even number of spin echo periods must be used to obtain a degree of compensation for refocusing pulse imperfections.

The in-phase S_x operator evolves partially into the antiphase operator $2I_zS_y$ under the scalar coupling Hamiltonian during τ_{cp}. The relaxation rate constant for heteronuclear antiphase magnetization includes a contribution from longitudinal relaxation of the coupled ^1H spin and thus is greater than the rate constant for in-phase magnetization (Section 5.4.2). Assuming that the initial density operator at the beginning of a spin echo period is proportional to S_x and $\pi J_{IS} \gg R_2$, then the phenomenological transverse relaxation rate constant measured in a CPMG experiment is given by

$$R_2(\tau_{cp}) \approx R_2 + \varepsilon R_{ext}, \qquad [8.19]$$

in which R_{ext} is the longitudinal relaxation rate constant for dipole–dipole interactions of the $^1H^N$ spin with remote ^1H spins and $\varepsilon = 0.5$ $[1 - \mathrm{sinc}[2\pi J_{IS}\tau_{cp})]$. Parenthetically, if the initial density operator is proportional to $2I_zS_y$, then the phenomenological relaxation rate constant is obtained by substituting $1 - \varepsilon$ for ε in [8.19]. To minimize contributions from antiphase magnetization to R_2, $\tau_{cp} < 1/(4J_{IS})$; typically, values of $\tau_{cp} \leq 1$ ms are utilized.

CPMG measurements of R_2 also are affected by off-resonance effects due to rotation of magnetization components (and consequent introduction of a degree of R_1 relaxation) during the refocusing pulses (*38, 39*). Numerical calculations suggest that systematic decreases in R_2 in the range of 3–10% are possible. To minimize these errors, the refocusing pulse length should be as short as possible and $< 10\%$ of the spin echo delay. Off-resonance effects can be corrected approximately by numerical simulations of the Bloch equations [1.28]. Measured values of R_1 and R_2 together with known values of ω_1 and Ω are used to simulate the magnetization decay curve. The apparent value of R_2

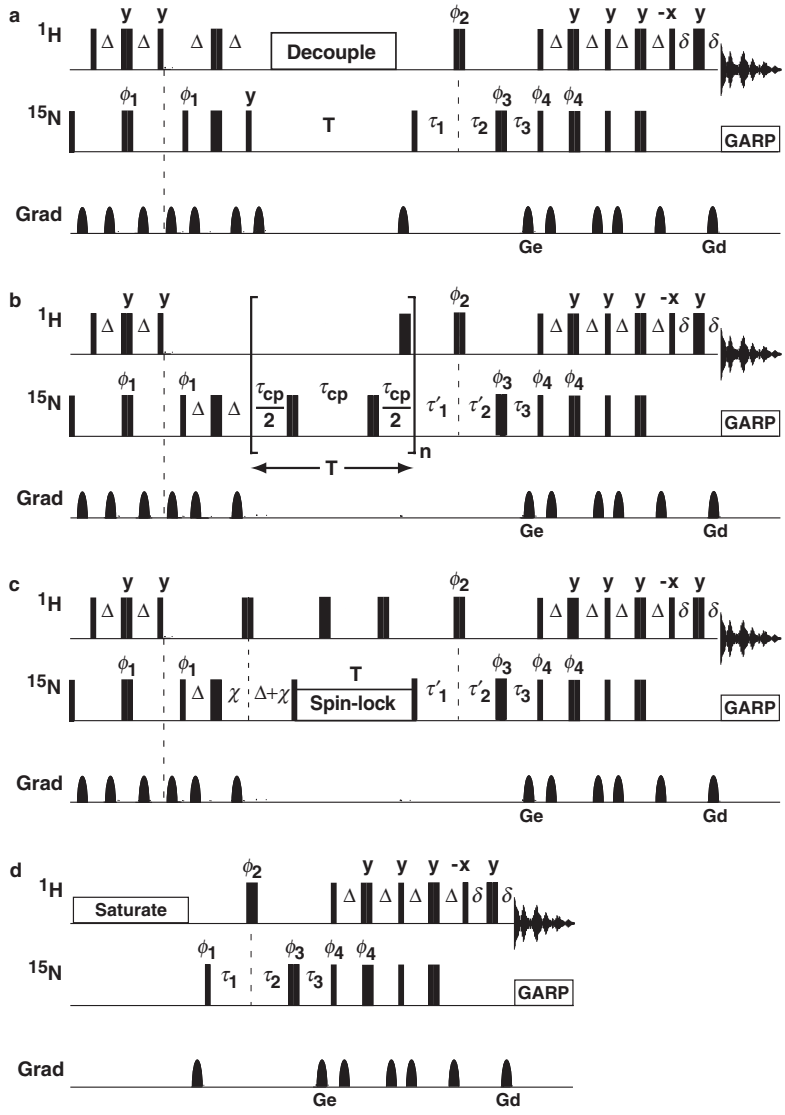

FIGURE 8.1 Pulse sequences for ^{15}N (a) R_1, (b) R_2, (c) $R_{1\rho}$, and (d) NOE spin relaxation measurements in ^{15}N backbone amide spin systems. R_1, R_2, and $R_{1\rho}$ intensity decay curves are recorded by varying the relaxation period T in a series of two-dimensional experiments. The NOE is measured by recording one spectrum with saturation of ^{1}H magnetization and one spectrum without saturation. Narrow and wide bars depict 90° and 180° pulses, respectively. All pulses are x-phase unless otherwise indicated. Decoupling during acquisition is

obtained from fitting the decay curve is used to correct the measured value (*38*).

In the $R_{1\rho}$ experiment shown in Fig. 8.1c, the initial density operator is proportional to S'_z, in which S'_z is the magnetization component locked along the direction of the effective field in the rotating frame of reference (Section 5.2.3). The initial density operator is created using a modified refocused INEPT sequence element. The $2I_zS_y$ magnetization created after the first S spin 90° pulse is converted to

$$S_x \cos(2\Omega\chi) + S_y \sin(s\Omega\chi) \qquad [8.20]$$

during the subsequent evolution periods. The 90° S spin pulse prior to T converts this density operator to

$$S_x \cos(2\Omega\chi) + S_z \sin(2\Omega\chi) = S'_z \qquad [8.21]$$

for $\chi = 1/(2\omega_1)$, in which ω_1 is the amplitude of the spin-locking rf field. This method relies on zthe identity $\tan\theta = \theta$ for small θ and is accurate to within 5% for $|\Omega/\omega_1| < 0.4$, corresponding to a tilt angle of $> 68°$. Alignment by means of an adiabatic sweep also is possible (see later,

FIGURE 8.1—*Continued*
achieved with the GARP-1 sequence (*117*). Decoupling during T in the R_1 experiment is performed using composite pulse decoupling or a train of ^{1}H 180° pulses. The R_2 CPMG experiment typically uses $\tau_{cp} = 1$ ms and $T = 2n\tau_{cp}$, in which n is an integer. Spin locking during the $R_{1\rho}$ experiment is performed using a continuous-wave rf field with amplitude ω_1 and frequency centered in the spectral range of interest. Saturation during the NOE experiment is performed using composite pulse decoupling or a train of ^{1}H 180° pulses. Delays are $\Delta = 1/(4J_{IS})$, $\chi = 1/(2\omega_1)$, $\tau_1 = \Delta + t_1/2$, $\tau_2 = (1 - 2\Delta/t_{1max})\ t_1/2$, $\tau_3 = (1 - t_1/t_{1max})\ \Delta$, t_{1max} is the maximum value of the t_1 labeling period, $\tau'_1 = \tau_1 + \chi$, $\tau'_2 = \tau_2 + \chi$, and $\delta >$ Gd. The delay χ is used to orient the initial magnetization along the direction of the effective field in the rotating reference frame (*118*). A semi-constant-time frequency-labeling period is used to increase resolution in the indirect dimension (*42, 43*). Conventional frequency labeling is obtained by setting $\tau_2 = t_1/2$ and $\tau_3 = \Delta$. The phase cycle is $\phi_1 = x, -x$; $\phi_2 = 4(x), 4(-x)$; $\phi_3 = x, x, y, y, -x, -x, -y, -y$; $\phi_4 = x$; receiver $= x, -x, -x, x$. The unlabeled gradients are used to suppress unwanted coherences and pulse imperfections (*119*). PEP gradient coherence selection is achieved with gradients Gd and Ge. Echo/antiecho signals are recorded in separate experiments by inverting the amplitude of Ge and phase ϕ_4 (*120*). The ϕ_1 and receiver phases are inverted for each t_1 increment to shift axial peaks to the edge of the spectrum (*121*).

Fig. 8.12c). Cross-relaxation due to ^1H–^{15}N DD/^{15}N CSA relaxation interference is suppressed by applying 180° ^1H pulses at $T/4$ and $3T/4$ (*40*). The intensity decay is described by

$$\langle S_z' \rangle(T) = \langle S_z' \rangle(0) \exp(-R_{1\rho} T). \quad [8.22]$$

The relaxation rate constants are corrected for the off-resonance tilted field using the expression

$$R_{1\rho} = R_1 \cos^2\theta + R_2 \sin^2\theta. \quad [8.23]$$

The steady-state NOE technique described briefly in Section 5.5 is used to measure the $\{^1H\}$–^{15}N NOE. The NOE experiment shown in Fig. 8.1d records two spectra, one with saturation of the ^1H spins and one without saturation during the recycle delay. Assuming that the recycle delay is $\gg 1/R_1$, in which R_1 is the spin–lattice relaxation rate constant for the ^{15}N spin, then the signal intensities in the two experiments are given by

$$\langle S_z \rangle_{\text{unsat}} = \langle S_z \rangle^0, \qquad \langle S_z \rangle_{\text{sat}} = (1 + \eta_{IS}) \langle S_z \rangle^0, \quad [8.24]$$

and the steady-state NOE is given by

$$\text{NOE} = \langle S_z \rangle_{\text{sat}} / \langle S_z \rangle_{\text{unsat}} = (1 + \eta_{IS}), \quad [8.25]$$

in which η_{IS} is the NOE enhancement [5.150]. Saturation is achieved with a composite pulse decoupling sequence such as WALTZ-16 or GARP-1. During the control experiment, a continuous-wave rf field of the same amplitude as the decoupling field strength is applied off-resonance to ensure that any heating effects are identical between experiments. The main concern in this experiment is that equilibrium magnetization must be restored in the control experiment. The $^1H^N$ and ^{15}N magnetizations are saturated at the beginning of the recycle delay; consequently, at a minimum, the recycle delay must be greater than $5/R_1$ to ensure that $>99\%$ of the equilibrium magnetization is restored. The NOE between the $^1H^N$ and ^{15}N spins couples the recovery of ^{15}N magnetization to that of $^1H^N$. In highly deuterated proteins, the $^1H^N$ R_1 may be significantly reduced and slow recovery of $^1H^N$ magnetization retards recovery of ^{15}N magnetization. Amide proton solvent exchange also complicates this experiment because the very small water ^1H, $R_1 = 0.25$ s^{-1} ($T_1 = 4$ s), is communicated to the $^1H^N$ spin by saturation transfer. Efficient water flip-back techniques are helpful in minimizing the degree of saturation transfer; however, even so, recycle delays $>3T_{1w}$ may be necessary to obtain

accurate results or the degree of saturation must be quantified empirically (*41*). Because the NOE experiment begins with ^{15}N magnetization, rather than a polarization transfer step from $^{1}H^{N}$ spins, the overall sensitivity of this experiment is much lower than the R_1 and R_2 experiments.

The pulse sequences shown in Fig. 8.1 use a semi-constant-time evolution period for frequency-labeling (*42, 43*) and PEP sequences for the mixing period. The semi-constant-time period provides some of the resolution advantages of a constant-time period, used extensively in Chapter 7, when suitably long delays do not naturally exist in the pulse sequence. As shown in Fig. 8.1, the total length of the evolution period is

$$\begin{aligned}\tau_1 + \tau_2 + \tau_3 &= \Delta + \frac{t_1}{2} + \left(1 - \frac{2\Delta}{t_{1\max}}\right)\frac{t_1}{2} + \left(1 - \frac{t_1}{t_{1\max}}\right)\Delta \\ &= 2\Delta + t_1\left(1 - \frac{2\Delta}{t_{1\max}}\right).\end{aligned} \quad [8.26]$$

When $t_1 = 0$, the evolution period has length 2Δ; when $t_1 = t_{1\max}$, the evolution period has length $t_{1\max}$. Evolution under the chemical shift Hamiltonian during the evolution period is given by

$$\tau_1 + \tau_2 - \tau_3 = \Delta + \frac{t_1}{2} + \left(1 - \frac{2\Delta}{t_{1\max}}\right)\frac{t_1}{2} - \left(1 - \frac{t_1}{t_{1\max}}\right)\Delta = t_1 \quad [8.27]$$

and evolution under the scalar coupling Hamiltonian is given by

$$\tau_1 - \tau_2 + \tau_3 = \Delta + \frac{t_1}{2} + \left(1 - \frac{2\Delta}{t_{1\max}}\right)\frac{t_1}{2} + \left(1 - \frac{t_1}{t_{1\max}}\right)\Delta = 2\Delta. \quad [8.28]$$

The values of these delays are incremented according to

$$\begin{aligned}\delta\tau_1 &= \delta t_1, \\ \delta\tau_2 &= \left(1 - \frac{2\Delta}{t_{1\max}}\right)\frac{\delta t_1}{2}, \\ \delta\tau_3 &= \frac{\Delta\delta t_1}{t_{1\max}},\end{aligned} \quad [8.29]$$

in which $\delta t_1 = 1/SW_1$ is the desired t_1 increment. Thus, the period 2Δ, required in the pulse sequence to evolve in-phase to antiphase magnetization, is utilized for t_1 frequency labeling as well. The effective

decay constant observed for the t_1 interferogram is

$$R_{2\text{eff}} = R_2(1 - 2\Delta/t_{1\text{max}}); \qquad [8.30]$$

consequently, a degree of resolution enhancement is obtained. The semi-constant-time approach can be adapted for many of the pulse sequences presented in the following sections and in Chapter 7. Conventional frequency labeling is obtained in the pulse sequences of Fig. 8.1 by setting $\tau_2 = t_1/2$ and $\tau_3 = \Delta$.

Examples of ^{15}N relaxation data for ubiquitin are shown in Fig. 8.2. The derived relaxation rate constants for ubiquitin are shown in Fig. 8.3. The median uncertainties in R_1, R_2, and NOE are 1.5%, 2.8%, and 2.8%, respectively.

8.2.2 EXPERIMENTAL METHODS FOR ^{15}N RELAXATION INTERFERENCE

Cross-relaxation due to ^{1}H–^{15}N DD/^{15}N CSA relaxation interference is suppressed in each of the preceding pulse sequences. Measurement of the ^{1}H–^{15}N DD/^{15}N CSA relaxation interference rate constant for transverse magnetization, η_{xy}, is useful for investigation of the variability of the CSA (*44, 45*) and for identifying sites subject to chemical exchange (*46*). A pulse sequence for measuring this rate constant is shown in Fig. 8.4. The initial density operator is proportional to $2I_zS_y$. This operator evolves into S_x coherence under the scalar coupling Hamiltonian. If $T = n/J_{IS}$, in which n is an integer, then the autorelaxation rate constants for in-phase and antiphase magnetization are averaged identically according to [8.19]. Consequently, the decay of magnetization is described by [8.12]. The experiment is performed twice. The first time, the intensity of the antiphase operator is recorded; the second time, the intensity of the in-phase operator, created by cross-relaxation, is recorded. The relaxation interference rate constant is calculated by [8.13]. Examples of η_{xy} for ubiquitin are shown in Fig. 8.4. The median uncertainty in η_{xy} is 1.1%; the larger scatter in the measured values, compared with R_2 (Fig. 8.2), arises from site-specific variation in the ^{15}N CSA (*44, 45*).

Other pulse sequences have been described for measuring CSA/dipole (*10, 17, 47, 48*), CSA/CSA (*49–51*), and dipole/dipole (*20*) relaxation interference rate constants. Use of relaxation interference relaxation rate constants to augment conventional R_1, R_2, and NOE measurements promises to significantly impact the information content of spin relaxation investigations of proteins.

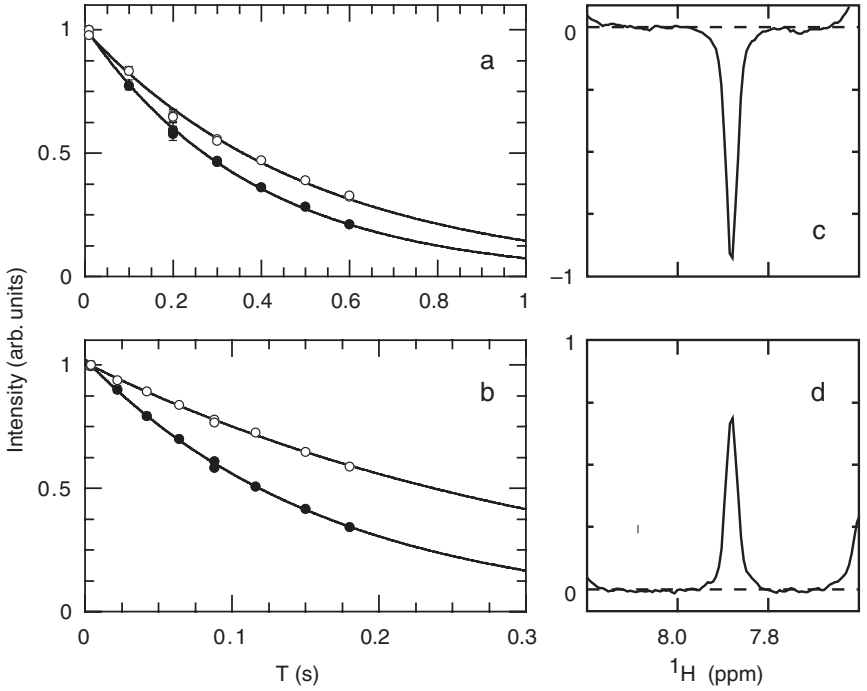

FIGURE 8.2 The ^{15}N relaxation data for ubiquitin recorded at 500 MHz and a temperature of 298 K. (a) R_1 intensity decays for residues Ile30 (•) in stable secondary structure and Arg74 (○) located near the C-terminus. Spectra were recorded with the pulse sequence of Fig. 8.1a. Solid lines are the best fits to [8.17], yielding $R_1 = 2.58 \pm 0.03$ and 1.87 ± 0.04 for Ile30 and Arg74, respectively. (b) R_2 intensity decays for residues Ile30 (•) and Arg74 (○). Spectra were recorded with the pulse sequence of Fig. 8.1b. Solid lines are the best fits to [8.18], yielding $R_2 = 5.98 \pm 0.07$ and 2.97 ± 0.08 for Ile30 and Arg74, respectively. (c) The slice parallel to the F_1 dimension is shown for residue Arg76 located at the C-terminus taken from the NOE (saturated) spectrum recorded with the pulse sequence of Fig. 8.1d. (d) The slice parallel to the F_1 dimension is shown for residue Arg76 taken from the control (unsaturated) spectrum recorded with the pulse sequence of Fig. 8.1d. The $\text{NOE} = -1.33 \pm 0.01$ is calculated from the ratio of the peak intensities according to [8.25].

8.2.3 EXPERIMENTAL METHODS FOR $^{13}CH_2D$ METHYL LABORATORY-FRAME RELAXATION

Experimental techniques have been developed to measure deuterium quadrupolar relaxation rate constants (see Chapter 5, Table 5.9) in

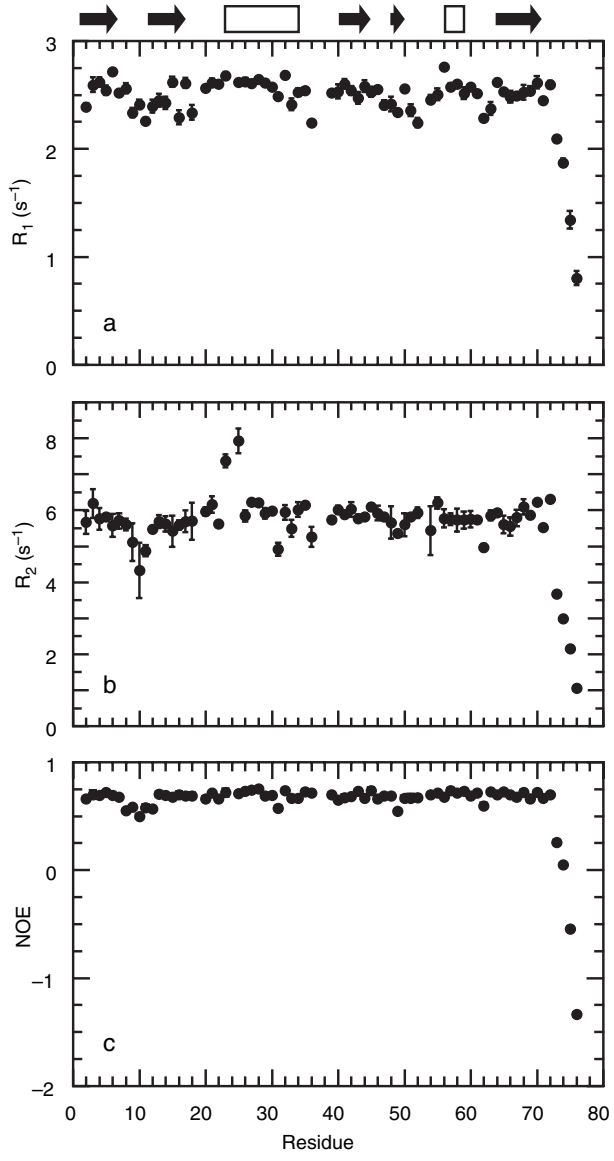

FIGURE 8.3 The ^{15}N relaxation rate constants for ubiquitin recorded at 500 MHz and a temperature of 298 K. Shown are (a) R_1, (b) R_2, and (c) NOE data as a function of residue position. The secondary structure of ubiquitin is depicted above the graphs, with β strands shown as filled arrows and α helices shown as open rectangles.

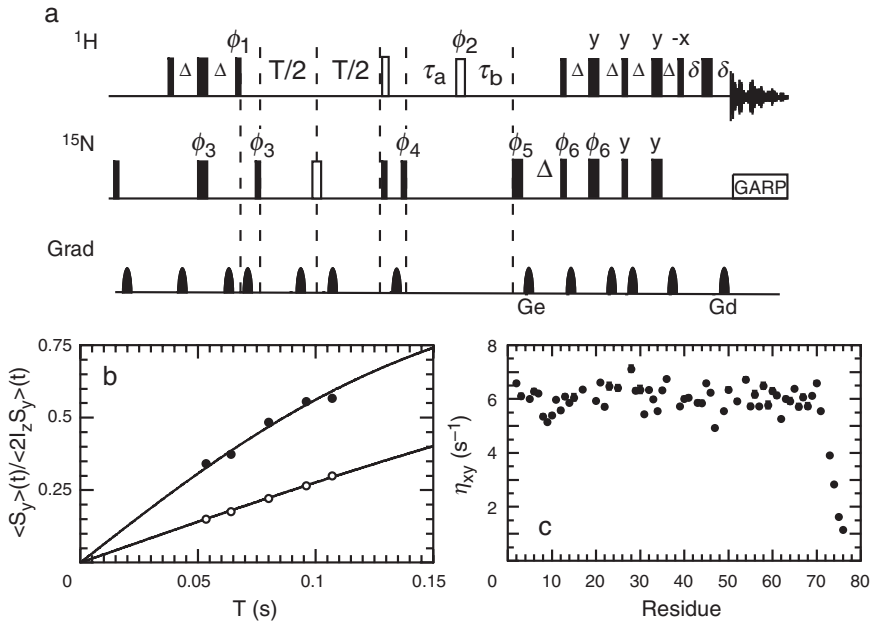

FIGURE 8.4 The ^{15}N CSA/^{1}H–^{15}N dipolar relaxation interference. (a) A pulse sequence for measuring η_{xy} is shown. Narrow and wide bars correspond to 90° and 180° pulses, respectively. Solid bars represent rectangular pulses while open bars correspond to composite $(90^\circ_x 90^\circ_y)$ 90° and composite $(90^\circ_y 90^\circ_x 90^\circ_y)$ 180° pulses. All pulses are applied with x-phase unless specified otherwise. Decoupling during acquisition is achieved with the GARP sequence (*117*). Delay durations are $\Delta = 1/(4J_{IS})$, $T = n/J_{IS}$, $\delta >$ Gd, and t_1 is the labeling period. Two experiments are performed for each value of the relaxation period T. In the first experiment, the composite ^{1}H 90° pulse, designated by the narrow open bar, is included, $\tau_a = \Delta$ and $\tau_b = \Delta + t_1/2$. In the second experiment, the composite 90° pulse is absent, $\tau_a = \Delta + t_1/2$ and $\tau_b = t_1/2$. The phase cycle is $\phi_1 = -y, -y, y, y$; $\phi_2 = 4(x), 4(-x)$; $\phi_3 = 4(x), 4(-x)$; $\phi_4 = 8(x), 8(-x)$; $\phi_5 = x, y, -x, -y$; $\phi_6 = x$; receiver $= x, -x, -x, x$, $2(-x, x, x, -x)$, $x, -x, -x, x$. The unlabeled gradients are used to suppress unwanted coherences and pulse imperfections. PEP gradient coherence selection is achieved with gradients Gd and Ge. Echo/antiecho signals are recorded in separate experiments by inverting the amplitude of Ge and phase ϕ_6 (*120*). The ϕ_3 and receiver phases are inverted for each t_1 increment to shift axial peaks to the edge of the spectrum (*121*). (b) Data are shown for residues Ile30 (•) in stable secondary structure and Arg74 (○) located near the C-terminus of ubiquitin. Solid lines are the best fits to [8.13], yielding $\eta_{xy} = 6.35 \pm 0.14$ s^{-1} and 2.84 ± 0.02 s^{-1} for Ile30 and Arg74, respectively. (c) Values of η_{xy} are shown as a function of residue position for ubiquitin. Data were recorded at 500 MHz and a temperature of 298 K.

$^{13}CH_2D$ methyl groups (*20, 52–54*). Pulse sequences for ^2H R_1 and $R_{1\rho}$ relaxation measurements are shown in Fig. 8.5 (*52*). The $R_{1\rho}$ technique is used to measure the spin–spin relaxation rate constant because short, high-quality ^2H 180° pulses necessary for CPMG methods are difficult to

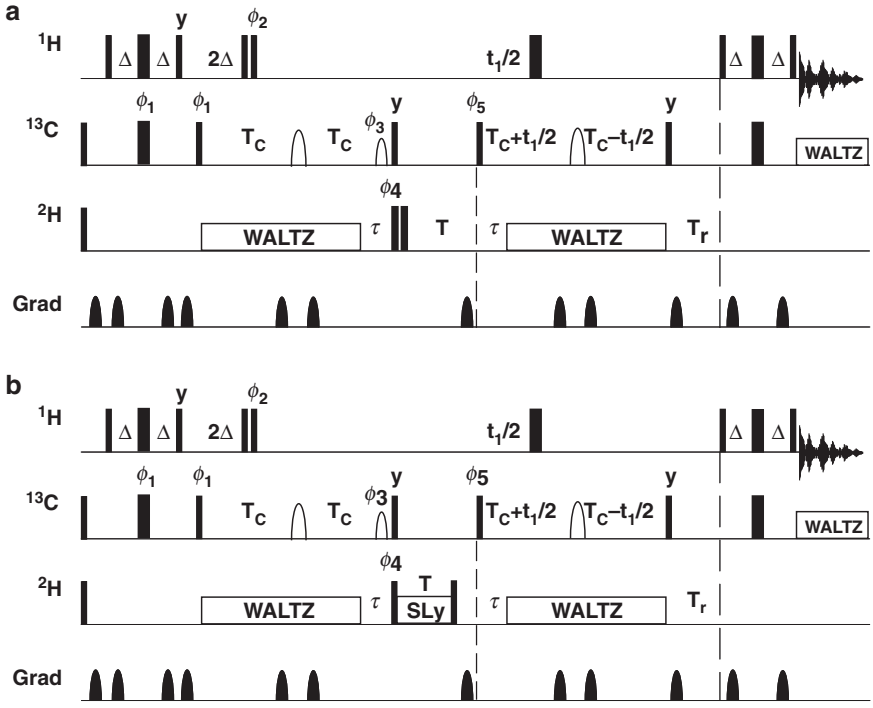

FIGURE 8.5 Pulse sequences for (a) R_1 and (b) $R_{1\rho}$ spin relaxation measurements in CH_2D spin systems ($D = {}^2H$). Intensity decay curves are recorded by varying the relaxation period T in a series of two-dimensional experiments. Narrow and wide bars depict 90° and 180° pulses, respectively; shaped pulses are shown as rounded bars. The 90° shaped pulse with phase cycle ϕ_3 is selective for the $^{13}C^{\alpha}$ spectral region. The 180° shaped pulses applied in the $2T_C$ constant-time periods are band selective for the aliphatic region of the ^{13}C spectrum. All pulses are x-phase unless otherwise indicated. Decoupling is achieved using WALTZ-16 (*122*). Delays are $\Delta = 1/(4J_{CH})$, $T_C = 1/(2J_{CC})$, $\tau = 1/(4J_{CD})$, $T_r = T_{max} - T$, T_{max} is the maximum value of T, and t_1 is the labeling period. The phase cycle is $\phi_1 = x, -x$; $\phi_2 = 2(x), 2(-x)$; $\phi_3 = x, -x$; $\phi_4 = 4(x), 4(-x)$; $\phi_5 = 8(x), 8(-x)$, receiver $= x, -x, -x, x, 2(-x, x, x, -x), x, -x, -x, x$. The unlabeled gradients are used to suppress unwanted coherences and pulse imperfections (*119*). Coherence selection is achieved with the TPPI–States scheme applied to ϕ_5 (*121*).

obtain on solution triple-resonance NMR probes. Pulse sequences for the relaxation rate constant for quadrupolar order, R_{1Q}, represented by the operator $3D_z^2 - 2$, and the relaxation rate constant for antiphase coherence, represented by the operator $D^+D_z + D_zD^+$, are shown in Fig. 8.6 (*53*). In each of these cases, the quadrupolar relaxation of the ^{2}H spin dominates relaxation, and other relaxation contributions are small (*52, 53, 55*). As discussed elsewhere, the relaxation rate constant for double-quantum coherence also can be measured experimentally; however, this relaxation rate constant contains contributions from other relaxation effects that require consideration (*53*). The ways in which ^{2}H and ^{13}C methods for investigating methyl group dynamics are used have been compared (*56, 57*). Similar approaches can be applied to ^{15}NHD amide moieties (*58*).

The experiments begin with an INEPT sequence to generate a density operator $2I_zS_y$. This operator evolves during the subsequent period $2T_C$ under the ^{1}H–^{13}C, ^{2}H–^{13}C, and ^{13}C–^{13}C scalar coupling Hamiltonians. The value of $2T_C = 1/J_{CC}$ so that the effects of the J_{CC} coupling are refocused. The value of $J_{CH} \gg J_{CD}$ (D = ^{2}H); consequently, after the delay 2Δ, the following operators are present:

$$\begin{aligned} C_x &\quad (\mathrm{CHD_2\ isotopomer}) \\ 2I_zC_y &\quad (\mathrm{CH_2D\ isotopomer}) \\ 4I_{iz}I_{jz}C_x &\quad (\mathrm{CH_3\ isotopomer},\ i \neq j) \end{aligned}$$

The operator present depends on the number of deuterons incorporated into the methyl group. The CH_2D isotopomers are selected by the 90°_x–$90^\circ_{\phi 2}$ pulse sandwich. Evolution under the J_{CD} scalar coupling Hamiltonian during the $2T_C$ period yields

$$I_zS_y \rightarrow I_zS_y\left(1 - D_z^2\right) + I_zS_yD_z^2 \cos[2\pi J_{CD}\tau] - I_zS_xD_z \sin[2\pi J_{CD}\tau]. \qquad [8.31]$$

The first term on the right-hand side of [8.31] represents the central line of the ^{13}C triplet and does not evolve under the scalar coupling Hamiltonian. The second and third terms represent the outer lines of the triplet that are either in-phase or antiphase with respect to the central line, respectively. Because τ is much shorter in the pulse sequences of Fig. 8.5 than of Fig. 8.6, increased sensitivity is obtained by using WALTZ-16 ^{2}H decoupling to maintain in-phase ^{13}C coherence for $2T_C - \tau$. This suppresses relaxation contributions from ^{2}H R_1 processes in the same manner that similar ^{1}H decoupling is used in decoupled HSQC and triple-resonance experiments (Chapter 7). The $^{13}C^\alpha$ selective

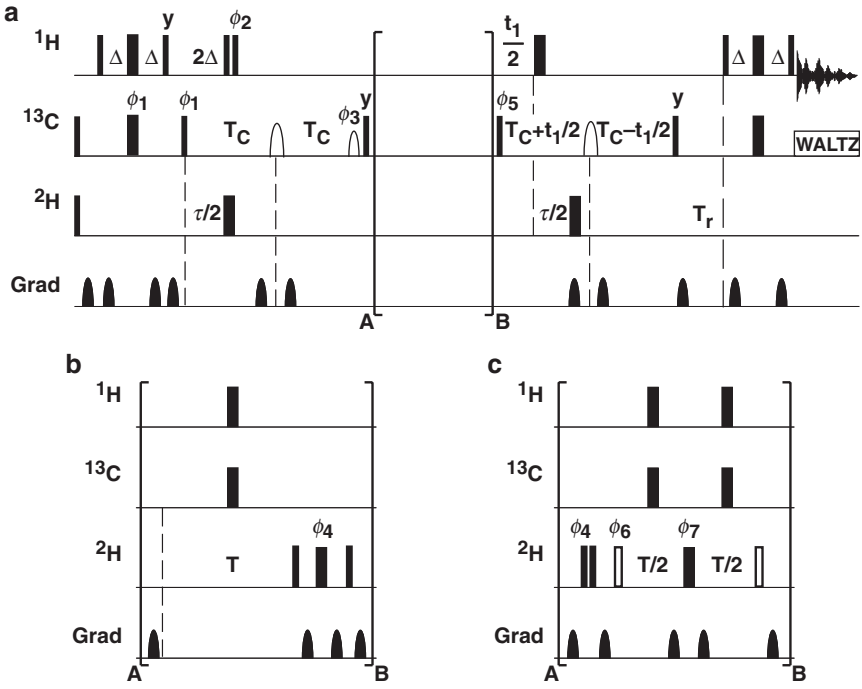

FIGURE 8.6 Pulse sequences for spin relaxation measurements for (b) quadrupolar order ($3D_z^2 - 2$) and (c) antiphase coherence ($D^+D_z + D_zD^+$), in CH_2D spin systems ($D = {}^2H$) obtained by inserting the bracketed segments into sequences in panel a. Intensity decay curves are recorded by varying the relaxation period T in a series of two-dimensional experiments. Narrow and wide bars depict 90° and 180° pulses, respectively; shaped pulses are shown as rounded bars. The 90° shaped pulse with phase cycle ϕ_3 is selective for the $^{13}C^{\alpha}$ spectral region. The 180° shaped pulses applied in the $2T_C$ constant-time periods are band selective for the aliphatic region of the ^{13}C spectrum. The rectangular open bar in panel c designates a 45° pulse. All pulses are x-phase unless otherwise indicated. Decoupling during acquisition is achieved using WALTZ-16 (*122*). Delays are $\Delta = 1/(4J_{CH})$, $T_C = 1/(2\ J_{CC})$, $\tau = 1/(2J_{CD})$, $T_r = T_{max} - T$, T_{max} is the maximum value of T, and t_1 is the labeling period. (b) The phase cycle is $\phi_1 = x, -x$; $\phi_2 = 2(x), 2(-x)$; $\phi_3 = x, -x$; $\phi_4 = 4(0°), 4(45°), 4(90°), 4(135°)$; $\phi_5 = 8(x), 8(-x)$; receiver $= x, -x, -x, x, 2(-x, x, x, -x), x, -x, -x, x$. (c) The phase cycle is $\phi_1 = x, -x$; $\phi_2 = 2(x), 2(-x)$; $\phi_3 = x, -x$; $\phi_4 = 4(x), 4(-x)$; $\phi_5 = 16(x), 16(-x)$; $\phi_6 = 8(x), 8(-x)$; $\phi_7 = 2(x), 2(-x)$; receiver $= 2(x, -x, -x, x), 4(-x, x, x, -x), 2(x, -x, -x, x)$. The unlabeled gradients are used to suppress unwanted coherences and pulse imperfections (*119*); relative signs of gradients to achieve optimal water suppression are discussed elsewhere (*53*). Coherence selection is achieved with the TPPI–States scheme applied to ϕ_3 (*121*).

pulse, with phase cycle ϕ_3, is used to suppress contributions from long-range ^{13}C–^{13}C scalar coupling interactions (*52, 53*).

In the R_1 and R_2 measurements, a density operator proportional to $I_zS_y(1-2D_z^2) - I_zS_xD_z$ is selected by setting $\tau = 1/(4J_{CD})$; only the desired operator $I_zS_xD_z$ is retained by the phase cycle of the ^2H $90^\circ_{\phi 4}$ pulse. For the other experiments, a density operator proportional to $I_zS_y(1-2D_z^2)$ is selected by setting $\tau = 1/(2J_{CD})$. In Fig. 8.6a, the $I_zS_yD_z^2$ operator is selected using a double-quantum filter following the relaxation period T. In Fig. 8.6b, the I_zS_y $(D^+D_z + D_zD^+)$ operator is generated by applying a 45° pulse to the $I_zS_y(1-2D_z^2)$ operator and contributions from other operators are suppressed by phase cycling ϕ_6 and ϕ_7.

The decay of magnetization during T contains contributions from relaxation of the I_zS_z operators as well as of the desired ^2H operators. For example, in the R_1 experiment, the relaxation of the $I_zS_zD_z$ operator is recorded, rather than the relaxation of D_z. These additional contributions are compensated by the $T_r = T_{max} - T$ period using the constant-relaxation-time approach (*59*). The effective relaxation decay for the entire pulse sequence is given by

$$I(T) = I(0)e^{-R_T T}e^{-R_{zz}(T_{max}-T)} = I(0)e^{-R_{zz}T_{max}}e^{-T(R_T-R_{zz})}, \qquad [8.32]$$

in which R_T is the effective relaxation rate constant during the period T and R_{zz} is the relaxation rate constant for $2I_zS_z$ two-spin order during T_r. The relaxation rate constant R_T is well approximated by the independent sum of the desired ^2H relaxation rate constant and R_{zz}. Consequently, the effective relaxation constant measured in these pulse sequences does not contain a contribution from R_{zz}. Finally, the operators D_z^2, and $(1-2D_z^2)$ have the same quadrupolar relaxation rate constants as for quadrupolar order, $3D_z^2-2$, because the identity operator does not contribute to relaxation, as shown by [5.70].

Examples of ^2H R_1 and $R_{1\rho}$ relaxation rate constants for ubiquitin are shown in Fig. 8.7. The median uncertainties in R_1 and R_2 are 6.1% and 5.5%, respectively.

8.2.4 EXPERIMENTAL METHODS FOR ^{13}CO LABORATORY-FRAME RELAXATION

Techniques have been reported for measurements of ^{13}C spin relaxation in carbonyl groups (*60–63*). The dipolar cross-relaxation rate constant between ^{13}CO and $^{13}C^\alpha$ spins, $\sigma_{C^\alpha CO}$, is unaffected by the ^{13}CO CSA or by dipolar interactions with ^1H spins and consequently is easier

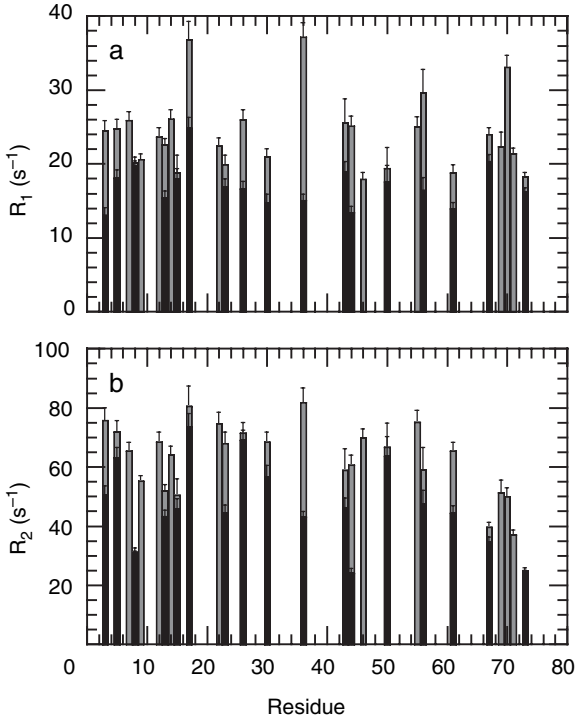

FIGURE 8.7 The ^{2}H relaxation rate constants for CH_2D methyl groups in ubiquitin (*56*). (a) R_1 and (b) $R_{1\rho}$ rate constants are shown as a function of residue position. Data were recorded at a field of 600 MHz and a temperature of 303 K. Data for Ile are shown as grey (black) bars for the γ (δ) methyl group; data for Leu are shown as grey (black) for the $\delta 1$ ($\delta 2$) methyl group, and data for Val are shown as grey (black) for $\gamma 1$ ($\gamma 2$) methyl group.

to interpret than are ^{13}CO R_1 or R_2 measurements (*64*). The cross-relaxation rate constant can be measured by a transient NOE experiment (*60*) or by a steady-state NOE measurement combined with an R_1 measurement (*63*). The latter approach is illustrated in Fig. 8.8. These experiments are based on the HNCO experiment (Section 7.4.4.1) and are similar in design to the ^{15}N R_1 and *NOE* experiments. The principal experimental consideration is that pulses used to saturate the $^{13}C^{\alpha}$ spins must be sufficiently band selective so as to leave the ^{13}CO spins unperturbed. Carbonyl relaxation is important for providing additional detail on backbone motions in proteins, because both the amide ^{15}N and the ^{13}CO spins report on motions of the peptide plane (*47, 65, 66*).

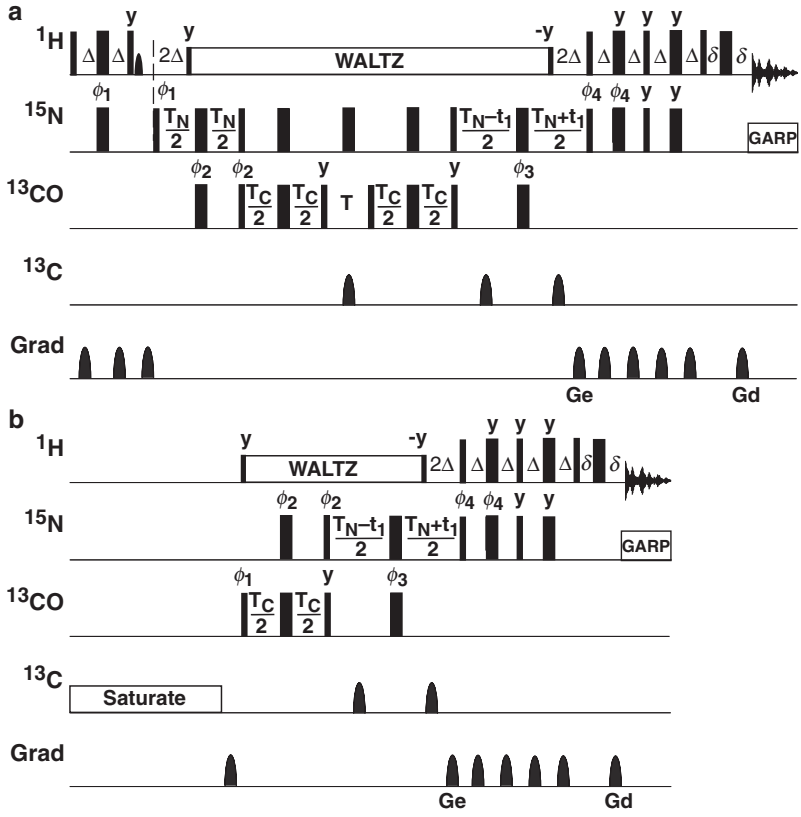

FIGURE 8.8 Pulse sequences for measuring ^{13}CO (a) R_1, and (b) $\{^{13}C^{\alpha}\}$–^{13}CO NOE. The R_1 intensity decay curves are recorded by varying the relaxation period T in a series of two-dimensional experiments. The NOE is measured by recording one spectrum with saturation of $^{13}C^{\alpha}$ magnetization and one spectrum without saturation. Narrow and wide bars depict 90° and 180° pulses, respectively; water flip-back pulses are shown as rounded bars (*123*). All pulses are x-phase unless otherwise indicated. Decoupling during acquisition is achieved with the GARP sequence (*117*); decoupling during T is performed using WALTZ-16 (*122*). Saturation during the NOE experiment is performed using a train of selective $^{13}C^{\alpha}$ pulses. Delays are $\Delta = 1/(4J_{NH})$, $T_N = 1/(4J_{NCO})$, $T_C = 1/(4J_{NCO})$, and $\delta >$ Gd. The phase cycle is $\phi_1 = x, -x$; $\phi_2 = 2(x), 2(-x)$; $\phi_3 = 4(x), 4(-x)$; $\phi_4 = x$; receiver $= x, -x, -x, x$. The unlabeled gradients are used to suppress unwanted coherences and pulse imperfections (*119*). PEP gradient coherence selection is achieved with gradients Gd and Ge. Echo/antiecho signals are recorded in separate experiments by inverting the amplitude of Ge and phase ϕ_4 (*120*). The ϕ_1 and receiver phases are inverted for each t_1 increment to shift axial peaks to the edge of the spectrum (*121*).

8.3 Microsecond–Second Dynamics

Techniques for probing microsecond–second time scale motions rely upon chemical exchange processes that modulate the isotropic chemical shift of ^{1}H, ^{13}C, and ^{15}N spins. The main techniques, ZZ-exchange (or NOESY) spectroscopy, CPMG relaxation dispersion, and $R_{1\rho}$ relaxation dispersion, are applicable to millisecond–second, millisecond, and microsecond–millisecond time scales, respectively. Classical lineshape analysis is applicable roughly to the same microsecond–millisecond time scales accessible to CPMG and $R_{1\rho}$ relaxation dispersion techniques. The basic theory of chemical exchange in NMR spectroscopy is described in Section 5.6. The simple two-site exchange mechanism is assumed throughout this section.

The initial step in characterizing a kinetic process by NMR spectroscopy is identifying spins subject to chemical exchange. If site populations are sufficiently large and exchange is slow on the chemical shift time scale, then additional resonances arising from the additional conformational or chemical states are observed in the NMR spectra. These resonances usually are identified during initial efforts to obtain sequence-specific resonance assignments. NOESY, ROESY, and ZZ-exchange spectroscopy, discussed in the following sections, are used to confirm that the additional resonances arise from chemical exchange processes. However, only a single set of resonances is observed in the NMR spectra if exchange is fast on the chemical shift time scale or if site populations are sufficiently low that the minor components are not observable in the slow exchange limit. In such circumstances, exchange effects are recognized by an increase in the transverse relaxation rate constant relative to the value expected for dipolar and CSA interactions for the observed resonance signals:

$$R_2 = \overline{R}_2^0 + R_{ex}, \qquad [8.33]$$

in which $\overline{R}_2^0$ refers to either the relaxation rate constant for an individual site (for slow exchange) or to the population-averaged relaxation rate constant (for fast exchange), and R_{ex} is the excess contribution to R_2 due to exchange. The exact relaxation rate constant for the dominant resonance signal is given by [5.183]. For fast exchange [5.186], $R_{ex} = p_1 p_2 \Delta\omega^2 / k_{ex}$ and, assuming $p_2 \leq 0.1$ and $\Delta\omega \leq 5000\ s^{-1}$, then $R_{ex} \geq 2.5\ s^{-1}$ for rates $k_{ex} < 10^6\ s^{-1}$. This result represents a rough upper bound on kinetic processes in proteins that can be characterized through methods based on chemical exchange broadening.

The value of R_2 in Eq. [8.33] can be approximated either by R_2^*, the free-precession damping constant including effects of magnetic field inhomogeneity, or by R_{2HE}, the damping constant observed for a Hahn spin echo experiment. The value of R_2^* is obtained from the resonance full-width at half-height linewidth, $\Delta\nu_{FWHH}$, using $R_2^* = \pi\Delta\nu_{FWHH}$, or equivalently, from the decay of the time-domain free induction decay or interferogram (in multidimensional NMR spectra) (*67*). The size of the inhomogeneity contribution to R_2^* can be estimated using spins not affected by the exchange process. The value of R_{2HE} is obtained using the sequence $T/2$–180°–$T/2$ incorporated into either a one-dimensional or a multidimensional NMR experiment (*68*). The 180° pulse must be selective to refocus homonuclear scalar coupling interactions, if any such interactions are significant. Usually, spectra are recorded for relaxation delays equal to 0 and T and then R_{2HE} is calculated using [8.10]. The echo time, T, should be long enough that $k_{ex}T \gg 1$; otherwise, the effects of exchange on the echo decay are partially suppressed. In either approach, additional decoupling sequences may need to be applied during the free-precession evolution period or during the spin echo delay to prevent evolution into antiphase coherences subject to additional relaxation mechanisms (*36, 37*).

An example of a pulse sequence for a WALTZ-16 decoupled Hahn echo experiment for ^{15}N spins is shown in Fig. 8.9. This experiment is very similar to the decoupled HSQC experiment (Section 7.1.1.3). The value of $T/4$ is adjusted so that an integral number of WALTZ-16 supercycles (Section 3.4.3) are performed in order to minimize effects of the decoupling sequence on the quality of the spin echo (*37, 69*).

The value of $\overline{R}_2^0$ in [8.33] is obtained by one of the following approaches: (*i*) analysis of R_1, R_2, and NOE data for ^{13}C or ^{15}N spins using the model-free formalism (*70, 71*), (*ii*) use of the magnetic field dependence of $R_2 - R_1/2$ to determine $J(0)$, the spectral density function at zero frequency (*72*), or (*iii*) use of ^{1}H–^{15}N DD/^{15}N CSA relaxation interference rate constants (*10, 45*). Using the last approach,

$$R_2^0 = \kappa\eta_{xy}, \qquad [8.34]$$

in which κ is a constant of proportionality that can be calculated theoretically using expressions in Chapter 5 (Tables 5.5 and 5.8 and [5.144]), or determined empirically for residues in the protein of interest known to be unaffected by chemical exchange processes. Values of R_{ex} determined from [8.33] and [8.34] are shown in Fig. 8.10. Values of R_{2HE} were determined using the experiment shown in Fig. 8.9, and values of

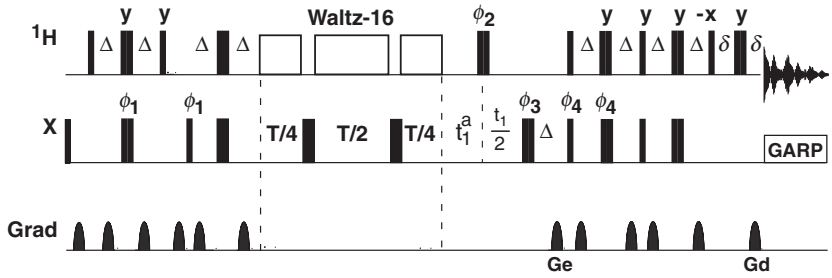

FIGURE 8.9 Pulse sequence for an in-phase Hahn echo pulse sequence for identifying chemical exchange in small to medium-sized proteins. The pulse sequence is applicable to isolated *IS* spin systems. Narrow and wide bars correspond to 90° and 180° pulses, respectively. All pulses are applied with *x*-phase unless specified otherwise. Decoupling during acquisition is achieved with the GARP sequence (*117*). Decoupling during the spin echo periods, shown as open boxes, is performed using WALTZ-16 (*122*). Delay durations are $\Delta = 1/(4J_{IS})$, $t_1^a = \Delta + t_1/2$, and $\delta >$ Gd. Two experiments are performed: once with $T = 0$ (and without WALTZ-16 decoupling) and once with $T/4$ chosen to be an integral number of WALTZ-16 supercycles. The phase cycling is $\phi_1 = -y, y$; $\phi_2 = x, x, -x, -x$; $\phi_3 = x, x, -x, -x$; $\phi_4 = x$; receiver $= x, -x, -x, x$. The unlabeled gradients are used to suppress unwanted coherences and pulse imperfections (*119*). PEP gradient coherence selection is achieved with gradients Gd and Ge. Echo/antiecho signals are recorded in separate experiments by inverting the amplitude of Ge and phase ϕ_4 (*120*). The ϕ_1 and receiver phases are inverted for each t_1 increment to shift axial peaks to the edge of the spectrum (*121*).

η_{xy} were taken from Fig. 8.4. Chemical exchange line broadening of the amide ^{15}N spins of residues 23, 25, 55, and 70 of ubiquitin is evident.

8.3.1 LINESHAPE ANALYSIS

Lineshape analysis is a classical approach for analyzing exchange processes in NMR spectroscopy (*73, 74*). Applications to proteins include chemical exchange arising from folding (*75–77*), ligand binding (*78–80*), and oligomerization (*81*). In each of these applications, the lineshapes can be altered by varying experimental parameters, such as temperature, ligand concentration, denaturant concentration, or protein concentration, which enables a global analysis of lineshapes to be performed as functions of the adjustable parameters. Typically, lineshape analysis is applicable to exchange processes in biological macromolecules with $k_{ex} \leq 10^5$ s^{-1}.

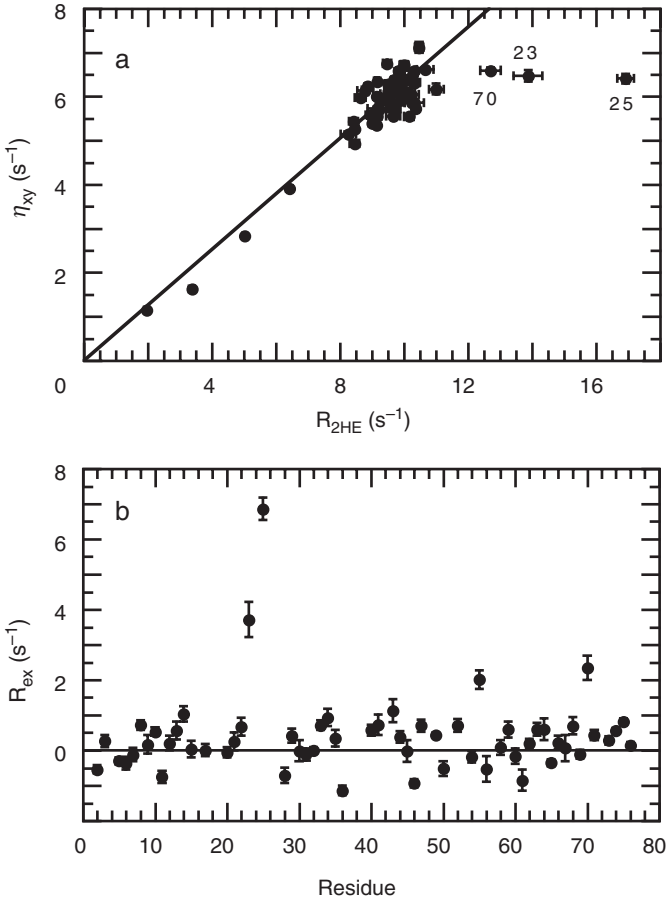

FIGURE 8.10 Values of ^{15}N R_{ex} for ubiquitin. (a) values of η_{xy} taken from Fig. 8.4 are plotted versus R_{2HE} determined using the experiment shown in Fig. 8.9 with $T = 57.9$ ms. (b) R_{ex} was calculated from [8.33] and [8.34] and an empirical value of $\kappa = 1.57$. Values of R_{ex} are shown as a function of residue position.

The NMR spectrum for an exchanging system is given by the Fourier transformation of [5.172] or [5.181]. Computer optimization of the parameters in these equations is utilized to fit the experimental lineshapes. In practical applications, particularly for ^1H lineshapes, the magnetization components should be regarded as representing individual resonance lines of scalar coupled multiplets. If scalar coupling

constants are modulated by the exchange process, then a more general theoretical approach based on a density operator formalism is required (*82*).

8.3.2 ZZ-EXCHANGE SPECTROSCOPY

Slow chemical exchange processes can be studied by monitoring the exchange of longitudinal magnetization between sites (Section 5.6.1) if the population of the minor site A_2 is large enough and exchange is slow enough to generate observable resonance signals for both sites A_1 and A_2 (*83*). In addition, k_{ex} must not be much less than R_1 for the exchanging sites; otherwise, the signals decay due to relaxation faster than population transfer. Investigations of chemical exchange using ^1H NMR spectroscopy are complicated by the coexisting transfer of magnetization through the nuclear Overhauser effect, although the opposite signs of the NOE and rotating-frame Overhauser effect (ROE) for macromolecules can be used to approximately suppress magnetization transfer through dipolar relaxation (*84*). Isotopic enrichment of macromolecules enables X-nucleus ZZ-exchange to be utilized instead of ^1H magnetization transfer. Longitudinal relaxation is much slower for ^{15}N and ^{13}C spins than for ^1H spins in macromolecules, and X-nucleus longitudinal magnetization is unaffected by ^1H–^1H cross-relaxation. Thus, although either exchange of longitudinal magnetization (*85, 86*) or two-spin order (*86, 87*) can be monitored, the relaxation rate constant for two-spin order is less favorable than for X-nucleus longitudinal magnetization. For biological macromolecules, X-nucleus R_1 values typically are on the order of 1 s^{-1}; consequently, ZZ-exchange measurements are applicable to chemical exchange processes with $1\ s^{-1} \leq k_{ex} \leq 10^3\ s^{-1}$.

A three-dimensional ^1H–X–^1H pulse sequence for a ZZ-exchange measurement is shown in Fig. 8.11; as described in the figure caption, either ^1H–^1H or X–^1H two-dimensional pulse sequences can be derived from the three-dimensional sequence and employed if the resonances due to exchanging spins are sufficiently well-resolved (*85, 88*). The evolution of longitudinal magnetization during the mixing time, T, is described by the modified Bloch–McConnell equations ([5.171] or [5.175]).

Cross-peak intensity can be observed at $T = 0$ if exchange is fast enough to transfer magnetization between sites during the INEPT periods. If ^1H magnetization is frequency labeled during t_1, then exchange effects must be considered between points A–B and C–D in Fig. 8.11. If only X magnetization is frequency labeled, during t_2, then exchange effects must be considered between points C–D in Fig. 8.11.

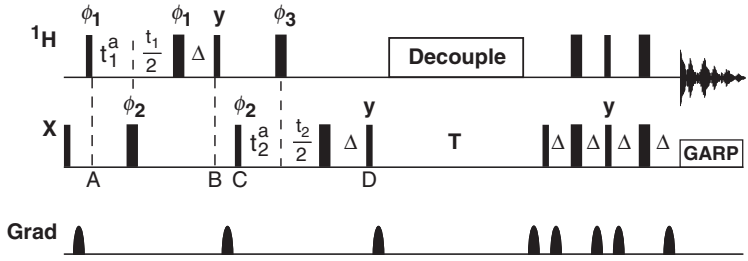

FIGURE 8.11 Pulse sequence for X nucleus ZZ-exchange NMR spectroscopy. The pulse sequence is applicable to isolated *IS* spin systems. Narrow and wide bars depict 90° and 180° pulses, respectively. All pulses are *x*-phase unless otherwise indicated. Decoupling during the relaxation delay to suppress heteronuclear dipole–dipole cross relaxation, and dipole/CSA cross-correlation can be performed using WALTZ-16 (*122*) or a train of ^{1}H 180° pulses at 5-ms intervals. Decoupling during acquisition is achieved with the GARP sequence (*117*). Delays are $\Delta = 1/(4J_{IS})$, $t_1^a = \Delta + t_1/2$, $t_2^a = \Delta + t_2/2$, and T is the mixing time. A two-dimensional X–^{1}H correlation spectrum is obtained by setting $t_1 = 0$; a two-dimensional ^{1}H–^{1}H correlation spectrum is obtained by setting $t_2 = 0$. The phase cycle is $\phi_1 = x, -x$; $\phi_2 = 4(x), 4(-x)$; $\phi_3 = x, x, y, y, -x, -x, -y, -y$; and receiver $= x, -x, -x, x$. The gradients are used to suppress unwanted coherences and pulse imperfections (*119*). Frequency discrimination is obtained by shifting the phase of the receiver, ϕ_1 and ϕ_2 according the TPPI–States protocol (*121*).

The effects of exchange during the INEPT periods can be approximated by including the length of the INEPT sequences, 2Δ, in the mixing time, provided that $|R_{11}^0 - R_{12}^0| \ll k_{ex}$ and $|R_{21}^0 - R_{22}^0| \ll k_{ex}$ for the X nucleus and $|R_{21}^0 - R_{22}^0| \ll k_{ex}$ for the ^{1}H spin, in which R_{1i}^0 and R_{2i}^0 are the spin–lattice and spin–spin relaxation rate constants for spins in the ith site. If these conditions do not hold, then the effects of exchange during the INEPT periods must be analyzed numerically. If a three-dimensional experiment is performed, then exchange during the t_2 evolution period must be analyzed numerically unless $t_{2max} k_{ex} \ll 1$.

8.3.3 $R_{1\rho}$ ROTATING-FRAME RELAXATION METHODS

In an $R_{1\rho}$ experiment, magnetization is spin-locked in the rotating frame by application of an rf field (*89, 90*). $R_{1\rho}$ experiments are sensitive to chemical exchange processes if values of ω_e near k_{ex} are achievable experimentally. Typically, $R_{1\rho}$ experiments are limited to

values of $k_{ex} \leq 10^5\ s^{-1}$. Sample heating and limitations on the maximum value of ω_1, usually $\leq 3 \times 10^4\ s^{-1}$ (5 kHz), tolerated by the spectrometer probe and amplifiers during sustained spin-locking pulses are the principal experimental constraints on ω_e. Furthermore, exchange processes with $k_{ex} > 10^6\ s^{-1}$ result in small exchange line broadening unless $\Delta\omega$ is very large. The $R_{1\rho}$ measurements on biological macromolecules can be performed using near-resonance (often called on-resonance for convenience) (*40, 91*) or off-resonance (*59, 92, 93*) rf fields. In the former case, the rf transmitter frequency is positioned close to the resonances of interest (or in the middle of the NMR spectrum) and the minimum value of ω_1 is large enough to ensure that $\theta > 68^\circ$ over the spectral region of interest. The relaxation dispersion curve is obtained by varying ω_1. In the latter case, the rf transmitter is positioned far enough off-resonance to ensure that $\theta < 68^\circ$. The relaxation dispersion curve is obtained by varying ω_1 or the carrier offset, or both, in order to vary ω_e.

Theoretical expressions for the $R_{1\rho}$ relaxation rate constant in the presence of chemical exchange have been presented elsewhere (*89, 90, 94–96*). For two-site chemical exchange in the fast-exchange limit (*89, 90*),

$$\begin{aligned} R_{1\rho} &= \overline{R}_1 \cos^2\theta + \overline{R}_2 \sin^2\theta \\ &= \overline{R}_1 \cos^2\theta + \overline{R}_2^0 \sin^2\theta + \sin^2\theta \frac{p_1 p_2 \Delta\omega^2 k_{ex}}{k_{ex}^2 + \omega_e^2}, \end{aligned} \qquad [8.35]$$

in which $\overline{R}_1$ and $\overline{R}_2^0$ are the population average relaxation rate constants in the absence of exchange. When site populations are highly skewed, $p_1 \gg p_2$, then (*95, 96*)

$$\begin{aligned} R_{1\rho} &= \overline{R}_1 \cos^2\theta + \overline{R}_2 \sin^2\theta \\ &= \overline{R}_1 \cos^2\theta + \overline{R}_2^0 \sin^2\theta + \sin^2\theta \frac{p_1 p_2 \Delta\omega^2 k_{ex}}{k_{ex}^2 + \omega_1^2 + \Omega_2^2} \end{aligned} \qquad [8.36]$$

is valid for all time scales. When [8.36] rather than [8.35] is applicable, relaxation dispersion depends on the resonance offset of the minor, usually unobservable, species. Thus, the value of Ω_2 can be determined from the resonance offset dependence of $R_{1\rho}$.

Pulse sequences for near-resonance (*40*) and off-resonance (*59, 92, 93*) $R_{1\rho}$ experiments for X spins are shown in Fig. 8.12. The near-resonance pulse sequence, Fig. 8.12a, is designed for rf field strengths as low as $\omega_1/(2\pi) = 1.7 J_{IS}$. To prevent evolution under an effective scalar coupling Hamiltonian, the ^1H 180° pulses used to decouple ^{15}N CSA/^1H–^{15}N dipolar relaxation interference are applied only when the

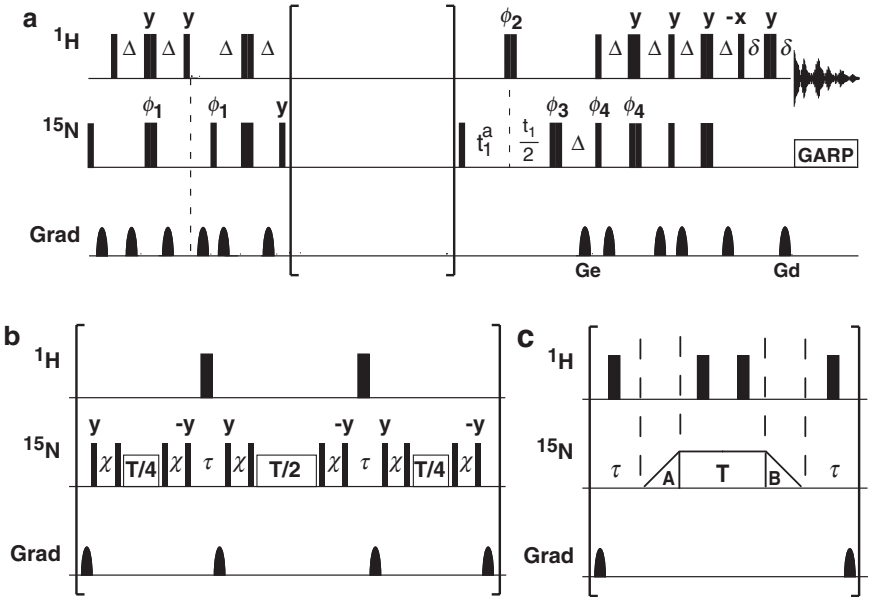

FIGURE 8.12 Pulse sequences for measuring ^{15}N $R_{1\rho}$ using (b) near-resonance and (c) off-resonance experiments obtained by inserting the bracketed segments into the sequence in panel a. Narrow and wide bars depict 90° and 180° pulses, respectively. All pulses are x-phase unless otherwise indicated. Decoupling during acquisition is achieved with the GARP sequence (*117*). Delays are $\Delta = 1/(4J_{IS})$, $t_1^a = \Delta + t_1/2$, T is the relaxation delay, and $\delta >$ Gd. For a constant-relaxation-time experiment, $\tau = (T_{max} - T)/2$; for a conventional experiment, τ is long enough to encompass any pulses and gradients. The 180° pulse during τ in panel c is omitted for a conventional experiment. (b) The spin lock rf frequency is positioned in the center of the spectral region of interest, and $\chi = 1/(2\omega_1)$ serves to align the magnetization along the direction of the effective field (*118*). (c) The spin lock rf frequency is set outside the spectral region of interest. The adiabatic sweep A rotates z-magnetization to the direction of the effective field and the adiabatic sweep B rotates the spin locked magnetization back to the z-axis. The phase cycle is $\phi_1 = x, -x$; $\phi_2 = 4(x), 4(-x)$; $\phi_3 = x, x, y, y, -x, -x, -y, -y$; $\phi_4 = x$; receiver $= x, -x, -x, x$. The unlabeled gradients are used to suppress unwanted coherences and pulse imperfections (*119*). PEP gradient coherence selection is achieved with gradients Gd and Ge. Echo/antiecho signals are recorded in separate experiments by inverting the amplitude of Ge and phase ϕ_4 (*120*). The ϕ_1 and receiver phases are inverted for each t_1 increment to shift axial peaks to the edge of the spectrum (*121*).

magnetization is stored along the z-axis. Gradient pulses following the 180° ^{1}H pulses are used to dephase any residual transverse coherences. For rf field strengths satisfying $\omega_1/(2\pi) > 2.7J_{IS}$, the $R_{1\rho}$ pulse sequence of Fig. 8.1c is satisfactory as well. The off-resonance pulse sequence, Fig. 8.12b, is identical to the $R_{1\rho}$ pulse sequence of Fig. 8.1c except that the magnetization is aligned along the direction of the off-resonance effective field before the spin-locking period and is returned to the z-axis after the spin-locking period using adiabatic sweeps (*92*).

The dependence of $R_{1\rho}$ on R_1 in [8.23] can be simplified by the constant-relaxation-time approach (*59*). If $\tau = (T_{\max} - T)/2$ in Fig. 8.12, then the effective relaxation rate constant is given by

$$R_{\text{eff}} = R_{1\rho} - R_1 = R_1 \cos^2\theta + R_2 \sin^2\theta - R_1 = (R_2 - R_1)\sin^2\theta. \quad [8.37]$$

Chemical exchange line broadening of the amide ^{15}N spins of residues 23, 25, 55, and 70 of ubiquitin has been identified from elevated values of transverse relaxation rate constants measured using CPMG (Fig. 8.3) and Hahn echo techniques (Fig. 8.10). A relaxation dispersion curve for residue 25 in ubiquitin is shown in Fig. 8.13.

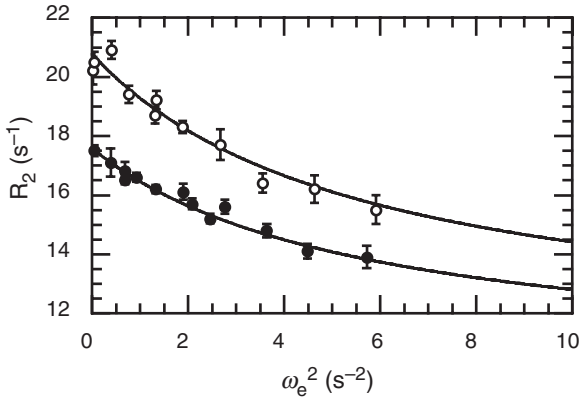

FIGURE 8.13 The ^{15}N $R_{1\rho}$ relaxation dispersion for residue Asn25 in ubiquitin (*124*). Values of R_2 were obtained from $R_{1\rho}$ using [8.23]. Data were recorded using both near-resonance and off-resonance pulse sequences shown in Fig. 8.12 at 500 MHz (○) and 600 MHz (●) at a temperature of 280 K. The solid line is the best fit of [8.35], yielding $k_{\text{ex}} = (2.3 \pm 0.2) \times 10^4$ s^{-1}.

8.3.4 CPMG RELAXATION METHODS

In a CPMG experiment, the relaxation of transverse magnetization is observed during a $(\tau-180^\circ-2\tau-180^\circ-\tau)_n$ spin echo sequence, in which $\tau_{cp}=2\tau$ is the spacing between 180° pulses and n is an integer (*33, 34*). CPMG experiments are sensitive to chemical exchange processes if values of $1/\tau_{cp}$ near k_{ex} are achievable experimentally. CPMG experiments in proteins typically are applicable to chemical exchange processes with values of $k_{ex} \leq 10^4$ s^{-1} as a result of experimental constraints on the minimum value of $\tau_{cp} \geq 0.1$–1 ms. Sample heating at high pulsing rates is a major experimental limitation. In addition, theoretical analyses of relaxation during CPMG experiments assume that the refocusing pulses have negligible duration (*97–99*); at pulse duty cycles >10%, this assumption may not be valid (*93*).

Theoretical expressions for the effective R_2 relaxation rate constant observed in a CPMG experiment in the presence of chemical exchange have been presented elsewhere (*89, 97, 98, 100*). For the case of two-site exchange, a general expression for the transverse relaxation rate constant for site 1 ($p_1 > p_2$), $R_2(1/\tau_{cp})$, is given by (*89*)

$$R_2\left(1/\tau_{cp}\right) = \overline{R}_2^0 + \frac{1}{2}\left(k_{ex} - \frac{1}{\tau_{cp}}\cosh^{-1}[D_+\cosh(\eta_+) - D_-\cos(\eta_-)]\right), \quad [8.38]$$

in which

$$D_\pm = \frac{1}{2}\left[\pm 1 + \frac{\psi + 2\Delta\omega^2}{(\psi^2+\zeta^2)^{1/2}}\right]^{1/2}, \qquad \eta_\pm = \frac{\tau_{cp}}{2}\left[\pm\psi + \left(\psi^2+\zeta^2\right)^{1/2}\right]^{1/2}, \quad [8.39]$$

where $\psi = k_{ex}^2 + \Delta\omega^2$ and $\zeta = -2\Delta\omega k_{ex}(p_1 - p_2)$. In the fast-exchange limit, [8.38] simplifies to

$$R_2\left(1/\tau_{cp}\right) = \overline{R}_2^0 + \frac{p_1 p_2 \Delta\omega^2}{k_{ex}}\left(1 - \frac{2\tanh\left[k_{ex}\tau_{cp}/2\right]}{k_{ex}\tau_{cp}}\right). \quad [8.40]$$

The maximum value of τ_{cp} for CPMG experiments applied to X spins is limited by evolution under the one-bond heteronuclear scalar coupling Hamiltonian, which interconverts in-phase and antiphase magnetization during the spin echo period [8.19]. The range of τ_{cp} values that can be utilized is expanded by CPMG experiments designed to

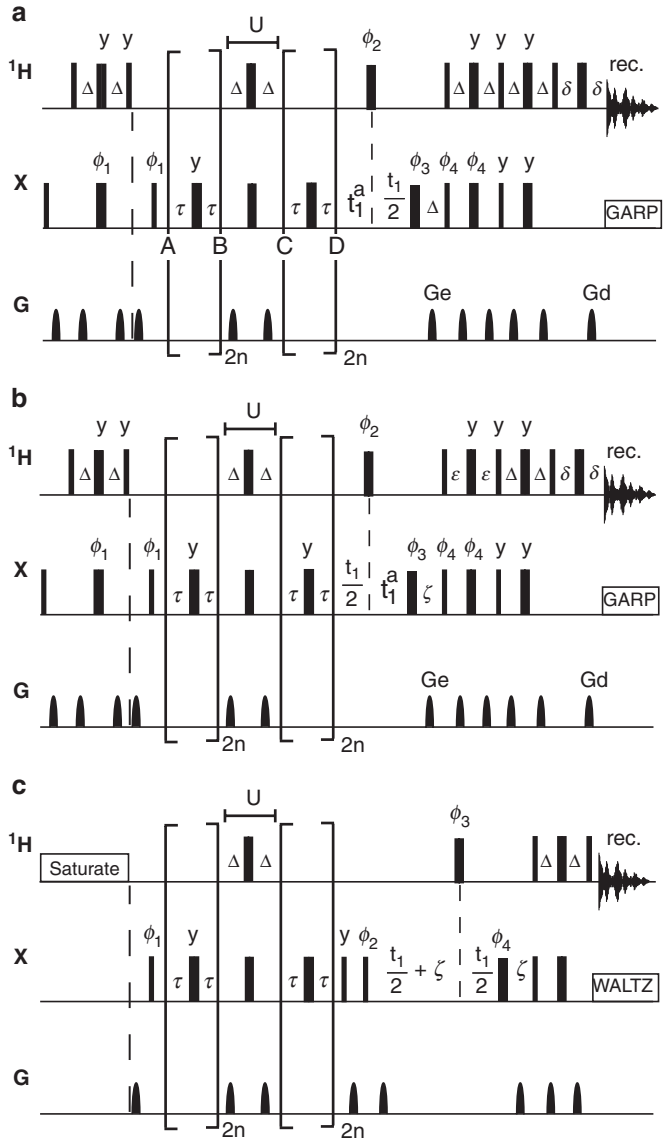

FIGURE 8.14 Pulse sequences for relaxation-compensated CPMG experiments in (a) *IS*, (b) I_2S, and (c) I_3S spin systems. Narrow and wide bars depict 90° and 180° pulses, respectively. All pulses are *x*-phase unless otherwise indicated. Decoupling during acquisition is achieved with the GARP or WALTZ-16 sequences (*117, 122*). Delays are $\tau = \tau_{cp}/2$, $\Delta = 1/(4J_{IS})$, and $\delta >$ Gd; (a) $t_1^a = \Delta + t_1/2$; (b) $\varepsilon = 1/(8J_{IS})$, $t_1^a = \zeta + t_1/2$, and $\zeta >$ Ge; (c) $\zeta = 1/(10J_{IS})$.

average in-phase and antiphase magnetization. Relaxation-compensated CPMG pulse sequences for *IS* (*101*), I_2S (*102*), and I_3S (*103*) are shown in Fig. 8.14. In these experiments, in-phase and antiphase coherences are interchanged during the period **U** in order to eliminate any τ_{cp}-dependent effects arising from differential relaxation rates.

The principles of the relaxation-compensated pulse sequences are illustrated for the simplest case of an *IS* spin system. The pulse sequence is shown in Fig. 8.14a. Following the initial INEPT period, the density operator at point A is proportional to $2I_zS_y$. Between points A and B, the relaxation of the density operator is described by [8.19], with $\varepsilon_{AB} = 0.5\ [1 + \text{sinc}[2\pi J_{IS}\tau_{cp})]$ (*36, 37*). The period **U** converts antiphase $2I_zS_y$ coherence to in-phase S_y coherence and suppresses CSA/dipolar cross-correlation to first order. Gradients G4 eliminate any imperfections in the 180° pulses, and the ^{1}H 90° pulse at the end of the **U** period converts any residual antiphase magnetization to multiple-quantum coherence, which is not detected. Between points C and D, the relaxation of the density operator is described by [8.19], with $\varepsilon_{CD} = 0.5\ [1 - \text{sinc}[2\pi J_{IS}\tau_{cp})]$. The total decay of the magnitude of the density operator between points A and D is given by

$$\begin{aligned} I(8n\tau_{cp}) &= I_0 \exp\left[-4n\tau_{cp}\left\{R_2(1/\tau_{cp}) + \varepsilon_{AB}R_{ext}\right\}\right] \\ &\quad \times \exp\left[-4n\tau_{cp}\left\{R_2(1/\tau_{cp}) + \varepsilon_{CD}R_{ext}\right\}\right] \\ &= I_0 \exp\left[-8n\tau_{cp}\left\{R_2(1/\tau_{cp}) + R_{ext}/2\right\}\right], \end{aligned} \qquad [8.41]$$

in which the efficiency of **U** is incorporated into I_0. Thus, the effective transverse relaxation constant for relaxation mechanisms other than chemical exchange is independent of τ_{cp}. After the final spin echo period, the magnetization is then frequency labeled during t_1 and returned back

FIGURE 8.14—*Continued*
Unlabeled gradients are used to suppress unwanted coherences and pulse imperfections (*119*). In panels a and b, the phase cycle is $\phi_1 = x, -x$; $\phi_2 = 4(x), 4(-x)$; $\phi_3 = x, x, y, y, -x, -x, -y, -y$; $\phi_4 = x$; receiver $= x, -x, -x, x$. Gradient coherence selection are achieved with gradients Gd and Ge. Echo/antiecho signals are recorded in separate experiments by inverting the amplitude of Gd and phase ϕ_4 (*120*). The ϕ_1 and receiver phases are inverted for each t_1 increment to shift axial peaks to the edge of the spectrum (*121*). In panel c, the phase cycle is $\phi_1 = x, -x$; $\phi_2 = 2(x), 2(-x)$; $\phi_3 = 8(x), 8(-x)$; $\phi_4 = 4(x), 4(y), 4(-x), 4(-y)$; receiver $= x, -x, -x, x, -x, x, x, -x$. Frequency discrimination during t_1 is obtained by shifting the phase of ϕ_2 and the receiver according the TPPI–States protocol (*121*).

to the I spins for detection by the refocused INEPT period. One drawback of the illustrated sequence is that the minimum relaxation delay is $4\tau_{cp}$. Conventional CPMG pulse sequences for measuring R_2 are self-compensating for evolution of the scalar coupling if $\tau_{cp} = m/J_{IS}$, in which m is an integer (*104*). Hahn spin echo measurements, self-compensated CPMG experiments, and relaxation-compensated CPMG experiments can be used in combination to cover the widest possible range of τ_{cp} values (*104*).

For I_2S and I_3S spin systems, relaxation is multiexponential and constant-relaxation-time experiments are necessary to obtain accurate results (*102, 103*). In this approach, relaxation rate constants are determined from measurements recorded with a relaxation delay of 0 and T using [8.10]. The relaxation dispersion curve is generated by varying τ_{cp} such that T is constant. If relaxation is multiexponential due to, for example, multiple dipole–dipole interactions, then

$$\langle A\rangle(T) = \exp\left[-R_{ex}\left(1/\tau_{cp}\right)T\right] \sum_j a_j \exp\left[-R_j T\right]\langle A\rangle(0), \qquad [8.42]$$

in which a_i and R_i are the amplitude and rate constant for the ith term in the multiexponential expansion, respectively, and $R_{ex}(1/\tau_{cp})$ is the exchange damping constant, given, for example, by $R_2\left(1/\tau_{cp}\right) - \overline{R}_2^{\,0}$ in [8.38]–[8.40]. Thus, using [8.10], an effective relaxation rate constant is defined:

$$\begin{aligned} R_{eff}\left(1/\tau_{cp}\right) &= (1/T)\ln[\langle A\rangle(0)/\langle A\rangle(T)] \\ &= R_{ex}\left(1/\tau_{cp}\right) - (1/T)\ln\left[\sum_j a_j \exp\left[-R_j T\right]\right]. \end{aligned} \qquad [8.43]$$

The second term does not depend on τ_{cp} and consequently represents a constant offset to the relaxation dispersion curve and is determined as part of the curve-fitting analysis.

A pulse sequence for a relaxation-compensated CPMG experiment for ^{1}H spins is shown in Fig. 8.15 (*105*). This experiment is applicable to ^{1}H spins that do not have significant homonuclear scalar coupling interactions; for example, the $^3J_{H^NH^\alpha}$ scalar coupling interaction is eliminated in uniformly ^{15}N/^{2}H-enriched proteins. In this experiment, the ^{15}N frequency-labeling period is placed before the CPMG element. As a result, the ^{1}H spins relax as unlike spins, even in the limit of fast pulsing (*106*). In addition, any ROESY cross-peaks that do arise from cross-relaxation when pulsing is fast are not degenerate with the main HSQC peaks, unless the ^{15}N shifts are degenerate. This experiment is

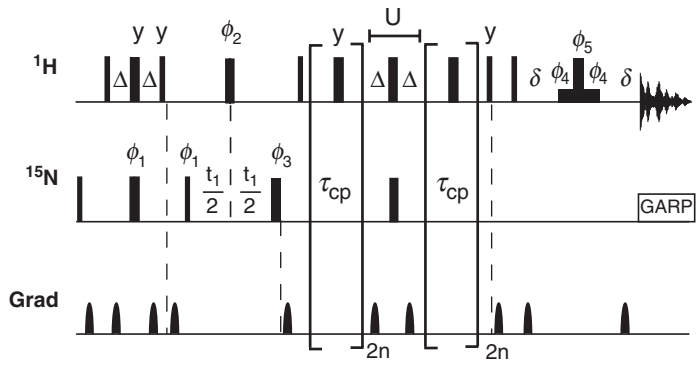

FIGURE 8.15 Pulse sequence for an amide ^{1}H CPMG experiment in ^{15}N/^{2}H-labeled proteins. Narrow and wide bars depict 90° and 180° pulses, respectively. All pulses are x-phase unless otherwise indicated. Decoupling during acquisition is achieved with the GARP or WALTZ-16 sequences (*117, 122*). Delays are $\Delta = 1/(4J_{IS})$, and δ is longer than the included gradients. Unlabeled gradients are used to suppress unwanted coherences and pulse imperfections (*119*). The phase cycle is $\phi_1 = x, -x$; $\phi_2 = 2(x), 2(-x)$; $\phi_3 = 8(x), 8(-x)$; $\phi_4 = 4(x), 4(y), 4(-x), 4(-y)$; receiver $= x, -x, -x, x, -x, x, x, -x$. Frequency discrimination during t_1 is obtained by shifting the phase of ϕ_1 and the receiver according the TPPI–States protocol (*121*).

performed using the constant-relaxation-time approach described previously to reduce the effects of multiexponential ^{1}H dipole–dipole relaxation on the measured dispersion curves.

8.3.5 CHEMICAL EXCHANGE IN MULTIPLE-QUANTUM SPECTROSCOPY

If two spins are affected by the same chemical exchange kinetic process, then the chemical shift changes for the two spins resulting from transitions between sites will be correlated. This correlation gives rise to exchange effects that can either broaden or narrow resonance lineshapes for multiple-quantum coherences (*107*). In essence, for multiple-quantum coherences, the value of $\Delta\omega$ in the equations given here and in Section 5.6 should be replaced by the difference in multiple-quantum (MQ) frequencies, $\Delta\omega_{MQ}$; thus, for double-quantum (DQ) and zero-quantum (ZQ) coherences, respectively, $\Delta\omega_{DQ} = \Delta\omega_I + \Delta\omega_S$ and $\Delta\omega_{ZQ} = \Delta\omega_I - \Delta\omega_S$, in which $\Delta\omega_I$ ($\Delta\omega_S$) is the chemical shift difference

between sites A_1 and A_2 for the I (S) spin. Hahn spin echo pulse sequences for measuring the difference between the relaxation rate constants for DQ and ZQ coherences have been developed for ^1H–^{15}N backbone amide moieties (*108*) and for $^{13}C^{\alpha}$–$^{13}C^{\beta}$ moieties (*109*) in proteins. In some cases, selection of the narrower of the DQ or ZQ coherences (depending on the relative chemical shifts) results in improved resolution and sensitivity of multidimensional NMR spectra (*107, 110*).

A pulse sequence for MQ relaxation in ^1H–^{15}N backbone amide moieties is shown in Fig. 8.16. The experiment creates $2I_yS_y$ coherence at the beginning of the relaxation period T and detects $2I_yS_y$ coherence in one experiment and $2I_xS_x$ coherence in the second experiment. The cross-relaxation rate constant is obtained from $\langle 2I_xS_x\rangle(T)/\langle 2I_yS_y\rangle(T)$ using [8.13]. The relaxation of these operators is described by

$$\frac{d}{dt}\begin{bmatrix}\langle 2I_xS_x\rangle(t)\\ \langle 2I_yS_y\rangle(t)\end{bmatrix} = -\begin{bmatrix}R_2 & \eta\\ \eta & R_2\end{bmatrix}\begin{bmatrix}\langle 2I_xS_x\rangle(t)\\ \langle 2I_yS_y\rangle(t)\end{bmatrix}. \qquad [8.44]$$

Recall from Section 2.7.5 that

$$\begin{bmatrix}\langle 2I_xS_x\rangle(t)\\ \langle 2I_yS_y\rangle(t)\end{bmatrix} = \begin{bmatrix}1 & 1\\ 1 & -1\end{bmatrix}\begin{bmatrix}\langle \mathrm{DQ}_x\rangle(t)\\ \langle \mathrm{ZQ}_x\rangle(t)\end{bmatrix} \qquad [8.45]$$

gives

$$\begin{aligned}\begin{bmatrix}R_2 & \eta\\ \eta & R_2\end{bmatrix} &= \frac{1}{2}\begin{bmatrix}1 & 1\\ 1 & -1\end{bmatrix}\begin{bmatrix}R_{\mathrm{DQ}} & 0\\ 0 & R_{\mathrm{ZQ}}\end{bmatrix}\begin{bmatrix}1 & 1\\ 1 & -1\end{bmatrix}\\ &= \begin{bmatrix}(R_{\mathrm{DQ}}+R_{\mathrm{ZQ}})/2 & (R_{\mathrm{DQ}}-R_{\mathrm{ZQ}})/2\\ (R_{\mathrm{DQ}}-R_{\mathrm{ZQ}})/2 & (R_{\mathrm{DQ}}+R_{\mathrm{ZQ}})/2\end{bmatrix}. \qquad [8.46]\end{aligned}$$

Thus, $2\eta = (R_{\mathrm{DQ}} - R_{\mathrm{ZQ}}) = \Delta R_{\mathrm{MQ}}$.

For two-site chemical exchange in the fast-exchange limit (*108*),

$$\Delta R_{\mathrm{MQ}} = R_{\mathrm{DQ}} - R_{\mathrm{ZQ}} = \overline{R}^0_{\mathrm{DQ}} - \overline{R}^0_{\mathrm{ZQ}} + 4p_1p_2\Delta\omega_I\Delta\omega_S/k_{\mathrm{ex}}, \qquad [8.47]$$

in which $\overline{R}_1$ and $\overline{R}^0_2$ are the population average relaxation rate constants in the absence of exchange. When $p_1 \gg p_2$, ΔR_{MQ} is given by (*2, 111*)

$$\Delta R_{\mathrm{MQ}} = \overline{R}^0_{\mathrm{DQ}} - \overline{R}^0_{\mathrm{ZQ}} + \frac{4p_1^2p_2\Delta\omega_I\Delta\omega_S k_{\mathrm{ex}}^3}{p_1^4k_{\mathrm{ex}}^4 + 2p_1^2k_{\mathrm{ex}}^2(\Delta\omega_I^2+\Delta\omega_S^2) + (\Delta\omega_I^2-\Delta\omega_S^2)^2} \qquad [8.48]$$

for all time scales. The difference $\overline{R}^0_{\mathrm{ZQ}} - \overline{R}^0_{\mathrm{DQ}}$ typically is small; consequently, the sign of ΔR_{MQ} gives the relative sign of the chemical

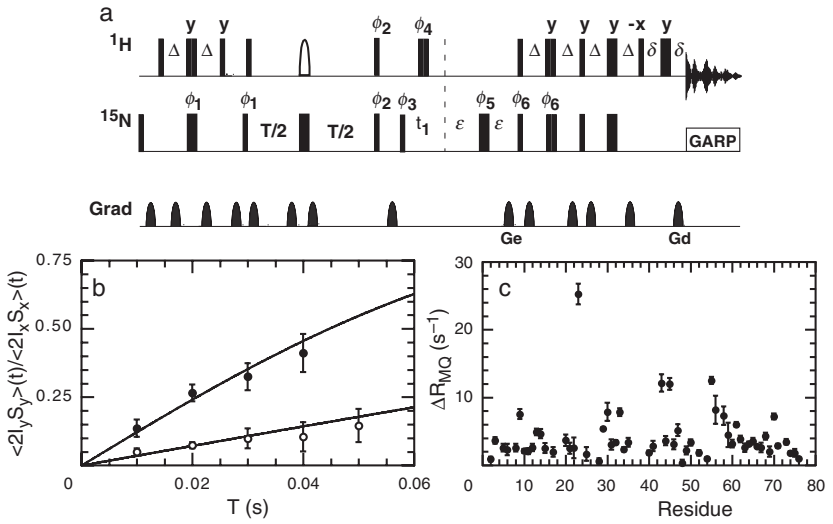

FIGURE 8.16 Multiple-quantum relaxation in ubiquitin. (a) Pulse sequence for measuring ^{1}H–^{15}N ΔR_{MQ}. Narrow and wide bars correspond to 90° and 180° pulses, respectively. All pulses are applied with x-phase unless specified otherwise. The shaped pulse is a band-selective 180° pulse centered on the amide ^{1}H spectral region. Delay durations are $\Delta = 1/(4J_{IS})$, $\delta >$ Gd, and, $\varepsilon >$ Ge. Two experiments are performed for each value of the relaxation period T. In the first experiment, $\phi_2 = y$, and $2I_xS_x$ magnetization is detected. In the second experiment, $\phi_2 = x$, and $2I_yS_y$ magnetization is detected. Decoupling is achieved with the GARP sequence during acquisition. The phase cycling is $\phi_1 = y, -y$; $\phi_3 = x, x, -x, -x$; $\phi_4 = x, x, -x, -x$; $\phi_5 = x$; receiver $= x, -x, -x, x$. The unlabeled gradients are used to suppress unwanted coherences and pulse imperfections (*119*). PEP gradient coherence selection is achieved with gradients Gd and Ge. Echo/antiecho signals are recorded in separate experiments by inverting the amplitude of Ge and phase ϕ_6 (*120*). The ϕ_1 and receiver phases are inverted for each t_1 increment to shift axial peaks to the edge of the spectrum (*121*). (b) Relaxation decay curves for residues 23 (•) and 70 (○) in ubiquitin, known to be subject to chemical exchange broadening (*124*). Data were recorded at 500 MHz and a temperature of 280 K. Solid lines are the best fits to [8.17], yielding $\Delta R_{MQ} = 25.2 \pm 1.5$ s^{-1} and 7.2 ± 0.4 s^{-1} for residues 23 and 70, respectively. (c) Values of ΔR_{MQ} are shown as a function of residue position.

shift differences for I and S spins (*108*). This information, which cannot be obtained from single-quantum experiments, is helpful for mechanistic interpretations of exchange phenomena.

Examples of the measurement of ΔR_{MQ} for ubiquitin are shown in Fig. 8.16. Residue 25 exhibits a large exchange broadening in SQ

experiments (Fig. 8.10), but a small value of ΔR_{MQ}; consequently, $\Delta\omega_H$ must be close to zero for the exchange process affecting this residue. In contrast, residue 23 shows large exchange broadening in both SQ and MQ experiments; consequently, both $\Delta\omega_H$ and $\Delta\omega_N$ must be significant.

For a heteronuclear spin system ($S = {}^{15}N$ or ${}^{13}C$ and $I = {}^{1}H$), the HMQC experiment records the average of the DQ and ZQ evolution frequencies, while the HSQC experiment records the single-quantum frequency (Section 7.1). When $p_1 \gg p_2$, the difference between the frequencies recorded in the HSQC and HMQC experiments is given by (*2, 112*)

$$\begin{aligned}\Delta\Omega &= \Omega_{HSQC} - \Omega_{HMQC} \\ &= \left[\frac{p_1 p_2 \Delta\omega_S \Delta\omega_I^2 k_{ex}^2}{p_1^2 k_{ex}^2 + \Delta\omega_S^2}\right]\left[\frac{3p_1^2 k_{ex}^2 + \Delta\omega_I^2 - \Delta\omega_S^2}{p_1^4 k_{ex}^4 + 2p_1^2 k_{ex}^2\left(\Delta\omega_I^2 + \Delta\omega_S^2\right) + \left(\Delta\omega_I^2 - \Delta\omega_S^2\right)^2}\right].\end{aligned} \quad [8.49]$$

As shown by Skrynnikov and co-workers (*112*), the second bracketed term is positive for a wide range of applicable parameters. Therefore, the sign of $\Delta\Omega$ is the same as the sign of $\Delta\omega_S$. Thus, provided that exchange is not in the fast limit, the sign of $\Delta\omega_S$ can be determined simply by comparing HSQC and HMQC spectra recorded under identical conditions.

8.3.6 TROSY-Based Approaches

Hahn echo (*113*) and CPMG (*106, 114, 115*) pulse sequences have been modified to select the narrow TROSY (Chapter 7) doublet component during the relaxation, indirect labeling, and detection periods. These modifications facilitate the quantification of exchange line-broadening contributions in larger macromolecules because the relative conformational exchange contribution to the phenomenological relaxation rate constant is enhanced and the improved resolution and sensitivity of TROSY ${}^{1}H$–${}^{15}N$ correlation spectra are obtained.

Fig. 8.17 shows a TROSY pulse sequence for measuring relaxation of the two scalar-coupled doublet components to simultaneously determine R_{ex} and η_{xy} (*113*). During the spin echo period of Fig. 8.17a, the signal intensities of the narrow and wide components

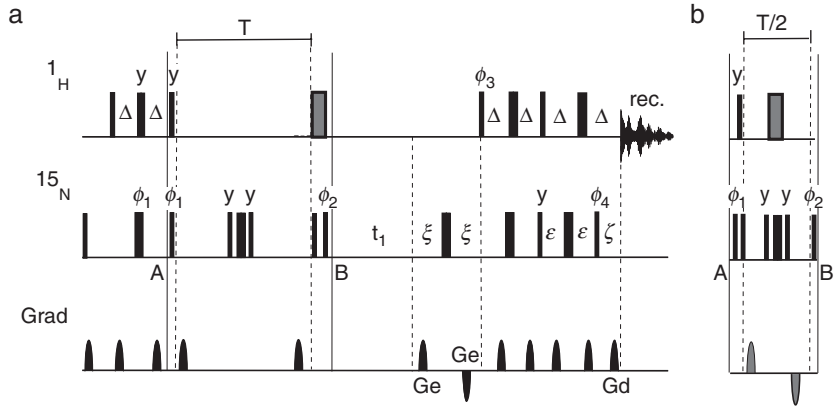

FIGURE 8.17 TROSY-based methods for detecting ^{15}N R_{ex} in large, deuterated proteins. The sequence shown in panel a detects relaxation of the narrow doublet component during the Hahn spin echo period $\tau_{he} = 2\tau$ when the grey pulse element is (90°_x 90°_y 90°_{-y} 90°_{-x}) and detects relaxation of the broad doublet component when this element is (90°_x 90°_y 90°_y 90°_x). Relaxation of longitudinal two-spin order is detected if the elements between points A and B in panel a are replaced with pulse elements in panel b; the gray element in panel b is (90°_x 90°_y 90°_y 90°_x). These pulses are applied at the center of the amide ^{1}H region to minimize off-resonance effects. Other delays are $\Delta = 1/4J_{IS}$, $\xi >$ Ge, $\varepsilon = \Delta - \zeta/2$, $\zeta >$ Gd. All pulses have x-phase unless otherwise stated. Phase cycles are $\phi_1 = x, -x$; $\phi_2 = x, x, -x, -x$; $\phi_3 = y$; $\phi_4 = x$; receiver phase $= -x, x, x, -x$. Gradients Ge and Gd are used for coherence selection; other gradients are for artifact suppression. Echo/antiecho quadrature detection is achieved by inverting ϕ_3, ϕ_4, and the sign of gradient Ge. The ϕ_1 and receiver phases are inverted for each t_1 increment to shift axial peaks to the edge of the spectrum (*121*).

of the ^{15}N doublet, $\langle S^+ I^\beta \rangle(T)$ and $\langle S^+ I^\alpha \rangle(T)$, respectively, decay according to

$$\begin{aligned} \langle S^+ I^\beta \rangle(T) &= I(0) \exp\left[-R_2^\beta T\right], \\ \langle S^+ I^\alpha \rangle(T) &= I(0) \exp\left[-\left(R_2^\beta + 2\eta_{xy}\right) T\right], \end{aligned} \qquad [8.50]$$

in which the initial intensity $I(0)$ is identical for both doublet components, and

$$R_2^\beta = \overline{R}_2^0 - \eta_{xy} + R_{ext}/2 + R_{ex}. \qquad [8.51]$$

Cross-relaxation between the two doublet components is suppressed by choosing $T = n/J_{IS}$, where n is a positive integer. The experiment is performed twice: once in which the signal $\langle S^+ I^\alpha \rangle(T)$ is detected and once in which the signal $\langle S^+ I^\beta \rangle(T)$ is detected. Thus,

$$\eta_{xy} = (1/2T)\ \ln\left[\langle S^+ I^\beta \rangle(T)/\langle S^+ I^\alpha \rangle(T)\right]. \qquad [8.52]$$

The relaxation rate constant $R_2^\beta - R_1^{2I_zS_z}/2$ is obtained by recording a third spectrum using the sequence shown in Fig. 8.17b. During the relaxation period of length $T/2$, the signal decays according to

$$\langle 2I_zS_z \rangle(T/2) = I(0)\ \exp\left[-R_1^{2I_zS_z}T/2\right]. \qquad [8.53]$$

Therefore,

$$R_2^\beta - R_1^{2I_zS_z}/2 = (1/T)\ \ln\left[\langle 2I_zS_z \rangle(T/2)/\langle S^+ I^\beta \rangle(T)\right]. \qquad [8.54]$$

The relaxation rate constant for two-spin order is given approximately by $R_1^{2I_zS_z} = R_1 + R_1^{\mathrm{H}}$. For proteins with a molecular mass >20 kDa, the ^{15}N R_1 is negligibly small. Thus, R_{ex} can be determined from

$$R_{\mathrm{ex}} = R_2^\beta - R_1^{2I_zS_z}/2 - (\kappa - 1)\eta_{xy}. \qquad [8.55]$$

A minimum of three two-dimensional NMR spectra are sufficient to determine R_{ex} using this approach.

Figure 8.18 shows a CPMG pulse sequence used for measuring ^{15}N $R_2^\beta(1/\tau_{\mathrm{cp}})$ as a function of τ_{cp} for the narrow component of the ^{1}H–^{15}N scalar-coupled doublet (*115*). The pulse sequence is designed to suppress cross-relaxation between the doublet components during the CPMG relaxation period, which would otherwise contribute to the apparent τ_{cp} dependence of the phenomenological relaxation rate constants. As shown by [5.146], the cross relaxation rate constant $\mu_0 = \left(R_{2I}^{\mathrm{DD}} - R_{2IS}^{\mathrm{DD}}\right)/2$ for free-precession evolution. In a CPMG experiment, the cross-relaxation rate constant also depends on τ_{cp} because the average overlap of the S^+I^α and S^+I^β operators depends on the relative phase angles acquired by the operators during the spin echo period (*37*). Thus, the effective cross-relaxation rate constant $\mu = \mu_0 \mathrm{sinc}(\pi J \tau_{\mathrm{cp}})$. In the limit where $\tau_{\mathrm{cp}} \to 0$, $\mu \to \mu_0$, and as $\tau_{\mathrm{cp}} \to \infty$, $\mu \to 0$. Suppression of the effects of cross-relaxation is achieved by the pulse sequence element **U**, which uses the S^3CT sequence element (*116*) to selectively invert one of the doublet components at a time $T/2$. Thus, **U** is given by [8.7] and the decay of magnetization is described by [8.8].

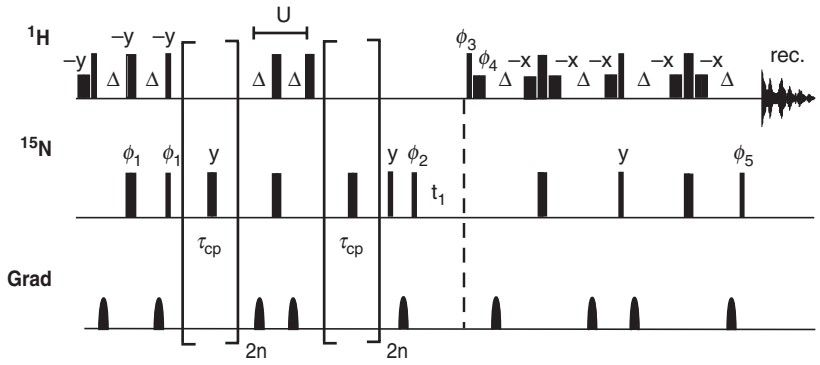

FIGURE 8.18 Pulse sequence for the ^{15}N TROSY–CPMG experiment. Narrow and wide bars depict 90° and 180° pulses, respectively. Short, solid bars are water-selective 90° pulses. All pulses are x-phase unless otherwise indicated. The delays are $\tau = \tau_{cp}/2$ and $\Delta = 1/(4J_{IS})$. The relaxation period is $T = 4n\tau_{cp}$. The data are acquired using the PEP scheme in which echo and antiecho FIDs are acquired for each t_1 point (*125*). The phase cycle for the first FID is $\phi_1 = 4(x)$, $4(-x)$; $\phi_2 = -y, y, x, -x$; $\phi_3 = y$; $\phi_4 = -y$; $\phi_5 = x$; receiver $= x, -x, y, -y, -x, x, y, -y$. The phase cycle for the second FID is $\phi_1 = 4(x)$, $4(-x)$; $\phi_2 = -y, y, x, -x$; $\phi_3 = -y$; $\phi_4 = y$; $\phi_5 = -x$; receiver $= -x, x, -y, y, x, -x, y, -y$. Gradients are used to suppress unwanted coherences and pulse imperfections (*119*) and perform water flip-back solvent suppression (*123*).

References

1. A. G. Palmer, J. Williams, A. McDermott, *J. Phys. Chem.* **100**, 13293–13310 (1996).
2. A. G. Palmer, *Chem. Rev.* **104**, 3623–3640 (2004).
3. P. Pelupessy, S. Ravindranathan, G. Bodenhausen, *J. Biomol. NMR* **25**, 265–280 (2003).
4. V. A. Daragan, K. H. Mayo, *Prog. NMR Spectrosc.* **31**, 63–105 (1997).
5. M. W. F. Fischer, A. Majumdar, E. R. P. Zuiderweg, *Prog. NMR Spectrosc.* **33**, 207–272 (1998).
6. L. E. Kay, *Nat. Struct. Biol.* **5**, 513–517 (1998).
7. A. G. Palmer, *Curr. Opin. Struct. Biol.* **7**, 732–737 (1997).
8. A. G. Palmer, C. D. Kroenke, J. P. Loria, *Meth. Enzymol.* **339**, 204–238 (2001).
9. A. G. Palmer, *Annu. Rev. Biophys. Biomolec. Struct.* **30**, 129–155 (2001).
10. C. D. Kroenke, J. P. Loria, L. K. Lee, M. Rance, A. G. Palmer, *J. Am. Chem. Soc.* **120**, 7905–7915 (1998).
11. J. A. Jones, *J. Magn. Reson.* **126**, 283–286 (1997).
12. G. H. Weiss, J. A. Ferretti, *Prog. NMR Spectrosc.* **20**, 317–335 (1988).
13. A. M. Mandel, A. G. Palmer, *J. Magn. Reson., Ser. A* **110**, 62–72 (1994).
14. L. E. Kay, J. H. Prestegard, *J. Magn. Reson.* **77**, 599–605 (1988).
15. P. A. Carr, D. A. Fearing, A. G. Palmer, *J. Magn. Reson.* **132**, 25–33 (1998).

16. G. Bodenhausen, R. R. Ernst, *J. Am. Chem. Soc.* **104**, 1304–1309 (1982).
17. N. Tjandra, A. Szabo, A. Bax, *J. Am. Chem. Soc.* **118**, 6986–6991 (1996).
18. P. Pelupessy, G. M. Espallargas, G. Bodenhausen, *J. Magn. Res.* **161**, 258–264 (2003).
19. B. Reif, M. Hennig, C. Griesinger, *Science* **276**, 1230–1233 (1997).
20. D. W. Yang, A. Mittermaier, Y. K. Mok, L. E. Kay, *J. Mol. Biol.* **276**, 939–954 (1998).
21. B. Reif, A. Diener, M. Hennig, M. Maurer, C. Griesinger, *J. Magn. Res.* **143**, 45–68 (2000).
22. N. A. Farrow, R. Muhandiram, A. U. Singer, S. M. Pascal, C. M. Kay, G. Gish, S. E. Shoelson, T. Pawson, J. D. Forman-Kay, L. E. Kay, *Biochemistry* **33**, 5984–6003 (1994).
23. A. C. Wang, A. Bax, *J. Biomol. NMR* **3**, 715–720 (1993).
24. J. Boyd, *J. Magn. Reson., Ser. B* **107**, 279–285 (1995).
25. K. T. Dayie and G. Wagner, *J. Magn. Reson., Ser. A*, **111**, 121–124 (1994).
26. N. J. Skelton, A. G. Palmer, M. Akke, J. Kördel, M. Rance, W. J. Chazin, *J. Magn. Reson. Ser. B* **102**, 253–264 (1993).
27. G. Zhu, Y. Xia, L. K. Nicholson, K. H. Sze, *J. Magn. Reson.* **143**, 423–426 (2000).
28. A. G. Palmer, M. Rance, P. E. Wright, *J. Am. Chem. Soc.* **113**, 4371–4380 (1991).
29. A. J. Wand, R. J. Bieber, J. L. Urbauer, R. P. McEvoy, Z. Gan, *J. Magn. Reson. Ser. B* **108**, 173–175 (1995).
30. D. M. LeMaster, D. M. Kushlan, *J. Am. Chem. Soc.* **118**, 9263–9272 (1996).
31. R. L. Vold, J. S. Waugh, M. P. Klein, D. E. Phelps, *J. Chem. Phys.* **48**, 3831–3832 (1968).
32. J. Boyd, U. Hommel, I. D. Campbell, *Chem. Phys. Lett.* **175**, 477–482 (1990).
33. H. Y. Carr, E. M. Purcell, *Phys. Rev.* **94**, 630–638 (1954).
34. S. Meiboom, D. Gill, *Rev. Sci. Instrum.* **29**, 688–691 (1958).
35. J. W. Peng, V. Thanabal, G. Wagner, *J. Magn. Reson.* **94**, 82–100 (1991).
36. L. E. Kay, L. K. Nicholson, F. Delagio, A. Bax, D. A. Torchia, *J. Magn. Reson.* **97**, 359–375 (1992).
37. A. G. Palmer, N. J. Skelton, W. J. Chazin, P. E. Wright, M. Rance, *Mol. Phys.* **75**, 699–711 (1992).
38. D. M. Korzhnev, E. V. Tischenko, A. S. Arseniev, *J. Biomol. NMR* **17**, 231–237 (2000).
39. A. Ross, M. Czisch, G. C. King, *J. Magn. Reson.* **124**, 355–365 (1997).
40. F. Massi, C. Wang, E. Johnson, M. Rance, A. G. Palmer, *J. Am. Chem. Soc.* **126**, 2247–2256 (2004).
41. D. Idiyatullin, V. A. Daragan, K. H. Mayo, *J. Magn. Res.* **153**, 138–143 (2001).
42. S. Grzesiek, A. Bax, *J. Biomol. NMR* **3**, 185–204 (1993).
43. T. M. Logan, E. T. Olejniczak, R. X. Xu, S. W. Fesik, *J. Biomol. NMR* **3**, 225–231 (1993).
44. D. Fushman, N. Tjandra, D. Cowburn, *J. Am. Chem. Soc.* **120**, 10947–10952 (1998).
45. C. D. Kroenke, M. Rance, A. G. Palmer, *J. Am. Chem. Soc.* **121**, 10119–10125 (1999).
46. C. Wang, A. G. Palmer, *Magn. Reson. Chem.* **41**, 866–876 (2003).
47. M. W. F. Fischer, L. Zeng, Y. Pang, W. Hu, A. Majumdar, E. R. P. Zuiderweg, *J. Am. Chem. Soc.* **119**, 12629–12642 (1997).
48. R. Ghose, K. Huang, J. H. Prestegard, *J. Magn. Reson.* **135**, 487–499 (1998).
49. T. J. Norwood, M. L. Tillett, L.-Y. Lian, *Chem. Phys. Lett.* **300**, 429–434 (1999).
50. M. Pellecchia, Y. Pang, L. Wang, A. V. Kurochkin, A. Kumar, E. R. P. Zuiderweg, *J. Am. Chem. Soc.* **121**, 9165–9170 (1999).
51. M. Tessari, G. W. Vuister, *J. Biomol. NMR* **16**, 171–174 (2000).
52. D. R. Muhandiram, T. Yamazaki, B. D. Sykes, L. E. Kay, *J. Am. Chem. Soc.* **117**, 11536–11544 (1995).
53. O. Millet, D. R. Muhandiram, N. R. Skrynnikov, L. E. Kay, *J. Am. Chem. Soc.* **124**, 6439–6448 (2002).

54. N. R. Skrynnikov, O. Millet, L. E. Kay, *J. Am. Chem. Soc.* **124**, 6449–6460 (2002).
55. D. Yang, L. E. Kay, *J. Magn. Reson., Ser. B* **110**, 213–218 (1996).
56. A. L. Lee, P. F. Flynn, A. J. Wand, *J. Am. Chem. Soc.* **121**, 2891–2902 (1999).
57. R. Ishima, A. P. Petkova, J. M. Louis, D. A. Torchia, *J. Am. Chem. Soc.* **123**, 6164–6171 (2001).
58. K. Pervushin, G. Wider, K. Wüthrich, *J. Am. Chem. Soc.* **119**, 3842–3843 (1997).
59. M. Akke, A. G. Palmer, *J. Am. Chem. Soc.* **118**, 911–912 (1996).
60. F. Cordier, B. Brutscher, D. Marion, *J. Biomol. NMR* **7**, 163–168 (1996).
61. K. Dayie, G. Wagner, *J. Am. Chem. Soc.* **119**, 7797–7806 (1997).
62. J. Engelke, H. Rüterjans, *J. Biomol. NMR* **9**, 63–78 (1997).
63. L. Zeng, M. W. F. Fischer, E. R. P. Zuiderweg, *J. Biomol. NMR* **7**, 157–162 (1996).
64. P. Allard, T. Härd, *J. Magn. Reson.* **126**, 48–57 (1997).
65. S. F. Lienin, T. Bremi, B. Brutscher, R. Brüschweiler, R. R. Ernst, *J. Am. Chem. Soc.* **120**, 9870–9879 (1998).
66. T. Wang, S. Cai, E. R. P. Zuiderweg, *J. Am. Chem. Soc.* **125**, 8639–8643 (2003).
67. M. Akke, J. Liu, J. Cavanagh, H. P. Erickson, A. G. Palmer, *Nat. Struct. Biol.* **5**, 55–59 (1998).
68. L. C. Wang, Y. X. Pang, T. Holder, J. R. Brender, A. V. Kurochkin, E. R. P. Zuiderweg, *Proc. Natl. Acad. Sci. U.S.A.* **98**, 7684–7689 (2001).
69. A. J. Shaka, J. Keeler, *Prog. NMR Spectrosc.* **19**, 47–129 (1987).
70. A. M. Mandel, M. Akke, A. G. Palmer, *J. Mol. Biol.* **246**, 144–163 (1995).
71. L. E. Kay, D. A. Torchia, A. Bax, *Biochemistry* **28**, 8972–8979 (1989).
72. I. Q. H. Phan, J. Boyd, I. D. Campbell, *J. Biomol. NMR* **8**, 369–378 (1996).
73. B. D. N. Rao, *Meth. Enzymol.* **176**, 279–311 (1989).
74. J. Sandstrom, "Dynamic NMR Spectroscopy." Academic Press, London, 1982.
75. R. E. Burton, R. S. Busby, T. G. Oas, *J. Biomol. NMR* **11**, 355–359 (1998).
76. M. E. Holtzer, G. L. Bretthorst, D. A. d'Avignon, R. H. Angeletti, L. Mints, A. Holtzer, *Biophys. J.* **80**, 939–951 (2001).
77. B. Kuhlman, D. L. Luisi, P. A. Evans, D. P. Raleigh, *J. Mol. Biol.* **284**, 1661–1670 (1998).
78. D. Kern, G. Kern, G. Scherer, G. Fischer, T. Drakenberg, *Biochemistry* **34**, 13594–13602 (1995).
79. U. Günther, T. Mittag, B. Schaffhausen, *Biochemistry* **41**, 11658–11669 (2002).
80. T. Mittag, B. Schaffhaussen, U. L. Günther, *J. Am. Chem. Soc.* **126**, 9017–9023 (2004).
81. D. S. Korchuganov, S. B. Nolde, M. Y. Reibarkh, V. Y. Orekhov, A. A. Schulga, Y. S. Ermolyuk, M. P. Kirpichnikov, A. S. Arseniev, *J. Am. Chem. Soc.* **123**, 2068–2069 (2001).
82. J. I. Kaplan, G. Fraenkel, "NMR of Chemically Exchanging Systems." Academic Press, New York, 1980.
83. J. J. Led, H. Gesmar, F. Abildgaard, *Meth. Enzymol.* **176**, 311–329 (1989).
84. J. Fejzo, Z. Zolnai, S. Macura, J. L. Markley, *J. Magn. Reson.* **88**, 93–110 (1990).
85. N. Farrow, O. Zhang, J. D. Forman-Kay, L. E. Kay, *J. Biomol. NMR* **4**, 727–734 (1994).
86. G. T. Montelione, G. Wagner, *J. Am. Chem. Soc.* **111**, 3096–3098 (1989).
87. G. Wider, D. Neri, K. Wüthrich, *J. Biomol. NMR* **1**, 93–98 (1991).
88. H. Wang, Y. Hea, C. D. Kroenke, S. Kodukulab, J. Storch, A. G. Palmer, R. E. Stark, *Biochemistry* **41**, 5453–5461 (2001).
89. D. G. Davis, M. E. Perlman, R. E. London, *J. Magn. Reson. Ser. B* **104**, 266–275 (1994).
90. C. Deverell, R. E. Morgan, J. H. Strange, *Mol. Phys.* **18**, 553–559 (1970).
91. T. Szyperski, P. Luginbühl, G. Otting, P. Güntert, K. Wüthrich, *J. Biomol. NMR* **3**, 151–164 (1993).

92. F. A. A. Mulder, R. A. de Graaf, R. Kaptein, R. Boelens, *J. Magn. Reson.* **131**, 351–357 (1998).
93. S. Zinn-Justin, P. Berthault, M. Guenneugues, H. Desvaux, *J. Biomol. NMR* **10**, 363–372 (1997).
94. D. Abergel, A. G. Palmer, *Concepts Magn. Reson.* **19A**, 134–148 (2003).
95. O. Trott, A. G. Palmer, *J. Magn. Reson.* **154**, 157–160 (2002).
96. O. Trott, D. Abergel, A. G. Palmer, *Mol. Phys.* **101**, 753–763 (2003).
97. A. Allerhand, E. Thiele, *J. Chem. Phys.* **45**, 902–916 (1966).
98. J. P. Carver, R. E. Richards, *J. Magn. Reson.* **6**, 89–105 (1972).
99. W. T. Sobol, *Magn. Reson. Med.* **21**, 2–9 (1991).
100. J. Jen, *J. Magn. Reson.* **30**, 111–128 (1978).
101. J. P. Loria, M. Rance, A. G. Palmer, *J. Am. Chem. Soc.* **121**, 2331–2332 (1999).
102. F. A. A. Mulder, N. R. Skrynnikov, B. Hon, F. W. Dahlquist, L. E. Kay, *J. Am. Chem. Soc.* **123**, 967–975 (2001).
103. N. R. Skrynnikov, F. A. A. Mulder, B. Hon, F. W. Dahlquist, L. E. Kay, *J. Am. Chem. Soc.* **123**, 4556–4566 (2001).
104. O. Millet, J. P. Loria, C. D. Kroenke, M. Pons, A. G. Palmer, *J. Am. Chem. Soc.* **122**, 2867–2877 (2000).
105. R. Ishima, D. A. Torchia, *J. Biomol. NMR* **25**, 243–248 (2003).
106. R. Ishima, P. T. Wingfield, S. J. Stahl, J. D. Kaufman, D. A. Torchia, *J. Am. Chem. Soc.* **120**, 10534–10542 (1998).
107. M. Rance, *J. Am. Chem. Soc.* **110**, 1973–1974 (1988).
108. K. Kloiber, R. Konrat, *J. Biomol. NMR* **18**, 33–42 (2000).
109. D. Fruh, J. R. Tolman, G. Bodenhausen, C. Zwahlen, *J. Am. Chem. Soc.* **123**, 4810–4816 (2001).
110. K. Pervushin, *J. Biomol. NMR* **20**, 275–285 (2001).
111. C. Wang, A. G. Palmer, *J. Biomol. NMR* **24**, 263–268 (2002).
112. N. R. Skrynnikov, F. W. Dahlquist, L. E. Kay, *J. Am. Chem. Soc.* **124**, 12352–12360 (2002).
113. C. Wang, M. Rance, A. G. Palmer, *J. Am. Chem. Soc.* **125**, 8968–8969 (2003).
114. J. Boisbouvier, B. Brutscher, J.-P. Simorre, D. Marion, *J. Biomol. NMR* **14**, 241–252 (1999).
115. J. P. Loria, M. Rance, A. G. Palmer, *J. Biomol. NMR* **15**, 151–155 (1999).
116. M. D. Sørensen, A. Meissner, O. W. Sørensen, *J. Biomol. NMR* **10**, 181–186 (1997).
117. A. J. Shaka, P. B. Barker, R. Freeman, *J. Magn. Reson.* **64**, 547–552 (1985).
118. T. Yamazaki, R. Muhandiram, L. E. Kay, *J. Am. Chem. Soc.* **116**, 8266–8278 (1994).
119. A. Bax, S. S. Pochapsky, *J. Magn. Reson.* **99**, 638–643 (1992).
120. L. E. Kay, P. Keifer, T. Saarinen, *J. Am. Chem. Soc.* **114**, 10663–10665 (1992).
121. D. Marion, M. Ikura, R. Tschudin, A. Bax, *J. Magn. Reson.* **85**, 393–399 (1989).
122. A. J. Shaka, J. Keeler, T. Frenkiel, R. Freeman, *J. Magn. Reson.* **52**, 335–338 (1983).
123. S. Grzesiek, A. Bax, *J. Am. Chem. Soc.* **115**, 12593–12594 (1993).
124. F. Massi, M. J. Grey and A. G. Palmer, *Protein Sci.* **14**, 735–742 (2005).
125. M. Rance, J. P. Loria, A. G. Palmer, *J. Magn. Reson.* **136**, 92–101 (1999).